

Quantum Process Tomography of the Quantum Fourier Transform

Yaakov S. Weinstein,^{1,*} Timothy F. Havel,¹ Joseph Emerson,^{1,†}
Nicolas Boulant,¹ Marcos Saraceno,² Seth Lloyd,³ and David G. Cory¹

¹*Massachusetts Institute of Technology,
Dept. of Nuclear Engineering, Cambridge, MA 02139, USA*

²*Unidad de Actividad Fisica, Tandem,
Comisión Nacional de Energía Atómica,
1429, Buenos Aires, ARGENTINA*

³*d'Arbelloff Laboratory for Information Systems and Technology,
Dept. of Mechanical Engineering, Massachusetts
Institute of Technology, Cambridge, MA 02139, USA*

Abstract

The results of quantum process tomography on a three-qubit nuclear magnetic resonance quantum information processor are presented, and shown to be consistent with a detailed model of the system-plus-apparatus used for the experiments. The quantum operation studied was the quantum Fourier transform, which is important in several quantum algorithms and poses a rigorous test for the precision of our recently-developed strongly modulating control fields. The results were analyzed in an attempt to decompose the implementation errors into coherent (overall systematic), incoherent (microscopically deterministic), and decoherent (microscopically random) components. This analysis yielded a superoperator consisting of a unitary part that was strongly correlated with the theoretically expected unitary superoperator of the quantum Fourier transform, an overall attenuation consistent with decoherence, and a residual portion that was not completely positive - although complete positivity is required for any quantum operation. By comparison with the results of computer simulations, the lack of complete positivity was shown to be largely a consequence of the incoherent errors during the quantum process tomography procedure. These simulations further showed that coherent, incoherent, and decoherent errors can often be identified by their distinctive effects on the spectrum of the overall superoperator. The gate fidelity of the experimentally determined superoperator was 0.64, while the correlation coefficient between experimentally determined superoperator and the simulated superoperator was 0.79; most of the discrepancies with the simulations could be explained by the cumulative effect of small errors in the single qubit gates.

PACS numbers: 03.67.Lx, 82.56.-b, 83.85.Ns

*Present address: Center for Computational Materials Science, Naval Research Laboratory, Washington, DC 20375, USA

†Present address: Perimeter Institute for Theoretical Physics, Waterloo, Ontario N2J 2W9, CANADA

I. INTRODUCTION

In order to develop larger and more powerful quantum information processing devices, it is essential to quantify the precision with which they can be controlled. This information is generally reported as a single number, the fidelity of the operation [1, 2, 3]. Although fidelity is a reasonable measure of control, it gives experimentalists little useful information about what went wrong or how to improve their control over the quantum system. Quantum process tomography (QPT) [5, 6, 7] provides additional information that may be useful in this regard, by yielding an estimate of the quantum operation that was actually implemented. This in turn provides a stringent check on the completeness and accuracy of the system-plus-apparatus model used to design the implementation. It is nevertheless a challenging task to interpret the deviations of this estimate from the superoperator implied by the model in terms of specific defects in the model. Additional errors introduced during the QPT procedure itself further complicate the analysis of the QPT results. In this paper we explore these issues via a concrete case study, in which QPT is performed on a previously reported three-qubit quantum Fourier transform (QFT) implemented using a nuclear magnetic resonance (NMR) quantum information processor [8].

The dynamics of an isolated quantum system are described by the Schrödinger equation, which gives rise to an $N \times N$ unitary operator, where N is the dimension of system's Hilbert space. Open quantum systems, however, generally interact with an inaccessible environment and thereby undergo decoherence [5]. Furthermore, in the case of expectation value measurements as in liquid-state NMR, each element of the statistical ensemble may undergo a slightly different unitary operation which, though nonrandom, is difficult to distinguish from decoherence [9, 10]. The statistics of measurements on open quantum systems are generally described by an $N \times N$ density operator, and the evolution of a density operator under an incoherent distribution of Hamiltonians and/or interactions with an environment, although non-unitary, remains linear and is described by a superoperator. The goal of quantum process tomography is to determine this superoperator.

Methods for implementing QPT have been presented Refs. [5, 6, 7, 12, 13], and two-qubit NMR implementations of QPT have previously been reported [14, 15]. In the present paper, QPT is carried out with the aim of validating the mathematical model of the system-plus-apparatus used to design the NMR implementation of a multi-qubit, entangling unitary

operation, and to identify the types and strengths of the errors that occurred. We have found it useful to classify the errors as coherent, incoherent, and decoherent, because each class is related to specific short-comings in the experimental implementation. Coherent errors are systematic errors in the net unitary operation that was actually implemented. Incoherent errors refer to unwanted unitary evolution which is not uniform across the ensemble of spin systems in the NMR sample, so that even though each member of the ensemble undergoes strictly unitary evolution, the evolution of the ensemble averages appears non-unitary. The effects of incoherence are reversible, at least in principle, and knowledge of the coherent and incoherent errors can be used to design better quantum gates (unitary operations). In contrast, decoherent errors are due to unknown interactions with an inaccessible environment, so they are not reversible and can be eliminated only by relatively costly changes to the apparatus or the way in which information is encoded within it.

An important benefit of QPT is that it poses a rigorous test of the accuracy of the mathematical model of the system-plus-apparatus used to design and interpret the experiments. This is done by comparing the experimental results of QPT to the results of computer simulations of the complete QPT procedure, based upon this same model. Simulations based on the model used here were also used in designing the strongly modulating control fields by which both the desired unitary operation as well as all the unitary operations needed for the QPT procedure were implemented [10]. This was done by minimizing the difference between the desired qubit rotation operator and the quantum operation obtained by simulating the effect of the control fields on the spins in the molecule used for the experiments. As a result, any incorrectness in the model directly affects the reliability of the experiments, but in ways that, by definition, differ from the simulations. This can suggest ways to improve the model, after which further simulations will pinpoint the remaining experimental errors.

The operation on which QPT was performed is the quantum Fourier transform (QFT). The QFT constitutes a key subroutine in several quantum algorithms [16, 17] as well as in certain methods for simulating quantum dynamics on a quantum computer [18, 19]. In algorithms such as Shor’s factoring algorithm, the QFT is used to extract periodic features of wave functions, while in simulations of quantum dynamics it is used to move between the position and momentum representations. The QFT is defined as follows:

$$U_{\text{QFT}}|x\rangle = \frac{1}{\sqrt{N}} \sum_{x'=0}^{N-1} e^{2\pi i x x'/N} |x'\rangle. \tag{1}$$

The QFT has been expressed [20, 21] as a sequence of one-qubit Hadamard gates H_j , which rotate the j th qubit from a computational basis state to an equal superposition of computational basis states, and two-qubit conditional phase gates $B_{jk}(\theta)$, which rotate the phase of qubit k by θ if qubit j is in the state $|1\rangle$. In this notation, the complete gate sequence of the three-qubit QFT is (reading from right-to-left)

$$\text{Swap}_{13} H_3 B_{23}\left(\frac{\pi}{2}\right) B_{13}\left(\frac{\pi}{4}\right) H_2 B_{12}\left(\frac{\pi}{2}\right) H_1 , \quad (2)$$

where Swap_{jk} is a swap gate between qubits j and k (see Fig. 1). This gate sequence has been implemented via NMR to demonstrate the ability of the QFT to extract periodicity [8], and as part of the quantum baker’s map [22].

The remainder of this paper is organized as follows. Section II gives an overview of the experimental and computational procedures used for QPT, together with the metrics by which the results were compared to those of the theoretical model. Section II describes incoherent errors and their effects on QPT, in particular the apparent lack of complete positivity of the results, while section III describes the experimental system and procedures used to implement QPT in detail. Section IV presents a complete description of the system-plus-apparatus model by which the results of QPT were interpreted. This is followed in section V by an overview of the experimental results, and in section VI by a detailed comparison of the results with the model’s predictions. Finally, section VII contains an analysis of the discrepancies between the experimental and simulated results, with the goal of determining their probable origins. The paper concludes with brief discussion of the implications of our findings for the field of quantum information processing as a whole.

II. QUANTUM PROCESS TOMOGRAPHY

There are several methods of performing QPT outlined in the literature. Some of these methods [7, 12] require increasing the Hilbert space size beyond that of the system whose dynamics are to be studied. This is unappealing for current experimental studies of quantum information processing where qubits are at a premium. The procedure used in this work (see Fig. 2) is similar to those given in Refs. [5, 6], and results in an $N^2 \times N^2$ complex-valued matrix, hereafter referred to as a “supermatrix.” Because of the inevitable experimental errors made in the QPT procedure, this supermatrix will not, in general, correspond to any

completely positive and trace-preserving superoperator (ergo quantum operation), unitary or otherwise. Therefore, we use methods recently introduced by Havel [13, 15] to obtain the best least-squares fit to the measured supermatrix that does correspond to such a quantum operation. This is expected to yield a better estimate of the superoperator that was actually implemented, since it will subsequently be shown that the non-completely positive part of the superoperator is largely due to errors committed during the readout steps.

The QPT procedure in Fig. 2 requires implementation of the desired unitary operation on a complete set of N^2 known input states, followed by determination of all of the resulting output states via quantum *state* tomography. Once all of the experimental input and output states have been completely determined, and given that the input states have been chosen to be linearly independent, the experimental supermatrix can be calculated as

$$\mathcal{M}_{\text{obs}} = \mathcal{R}_{\text{out}} \mathcal{R}_{\text{in}}^{-1}, \quad (3)$$

where \mathcal{R}_{in} and \mathcal{R}_{out} are supermatrices whose columns are the ‘‘columnized’’ experimental input and output density matrices $\text{col}(\rho_{\text{in}})$ and $\text{col}(\rho_{\text{op}})$, respectively, as determined by state tomography (see below). In quantum information processing, the Hilbert space is usually a tensor product of the 2-dimensional Hilbert spaces of its constituent qubits, so that $N = 2^n$ grows exponentially with the number of qubits n . As a result, QPT can in practice be carried out on only a few qubits at a time. Nevertheless, even a large quantum computer is expected to be based upon such local operations, so a complete analysis of small implementations is a prerequisite to understanding the issues involved in the control of larger systems.

We now introduce the measures of state and gate fidelities that were used to summarize the results of QPT. The accuracy with which the initial states were created was quantitated by the correlation between the desired input state and the one determined by state tomography [3], i.e.

$$C(\rho_{\text{th}}, \rho_{\text{in}}) = \frac{\text{tr}(\rho_{\text{th}}\rho_{\text{in}})}{\sqrt{\text{tr}(\rho_{\text{th}}^2)\text{tr}(\rho_{\text{in}}^2)}}, \quad (4)$$

where ρ_{th} and ρ_{in} are the traceless parts of the density matrices of the desired and measured input states, respectively. The input states were prepared from the equilibrium spin state by means of suitable non-unitary operations, \mathcal{S}_{in} , and the magnitudes of their traceless parts taken as the reference against which all subsequent losses of coherence (or magnetization in NMR) due to non-unitary evolution were measured. This was done by scaling the correlation of the output states by a factor which measures the loss of coherence [3], yielding the so-called

attenuated correlation

$$C_A(\rho_{\text{th}}, \rho_{\text{op}}) = C(\rho_{\text{th}}, \rho_{\text{op}}) \sqrt{\frac{\text{tr}(\rho_{\text{op}}^2)}{\text{tr}(\rho_{\text{in}}^2)}} , \quad (5)$$

where ρ_{th} and ρ_{op} are the traceless parts of the density matrices of the theoretical and measured output states, respectively, and ρ_{in} that of the corresponding input state from above.

The average state correlation and average attenuated state correlation are reasonable measures of the overall fidelity of the implemented quantum operation, but a measure that is more clearly independent of the choice of initial states is the correlation between the superoperator matrices, i.e.

$$C(\mathcal{S}_{\text{th}}, \mathcal{S}_{\text{op}}) \equiv \text{tr}(\mathcal{S}_{\text{th}}^\dagger \mathcal{S}_{\text{op}}) / \sqrt{\text{tr}(\mathcal{S}_{\text{th}}^\dagger \mathcal{S}_{\text{th}}) \text{tr}(\mathcal{S}_{\text{op}}^\dagger \mathcal{S}_{\text{op}})} . \quad (6)$$

Since this quantity is not sensitive to the overall loss of magnetization, we will also use the attenuated correlation between supermatrices, namely

$$C_A(\mathcal{S}_{\text{th}}, \mathcal{S}_{\text{op}}) \equiv \text{tr}(\mathcal{S}_{\text{th}}^\dagger \mathcal{S}_{\text{op}}) / \text{tr}(\mathcal{S}_{\text{th}}^\dagger \mathcal{S}_{\text{th}}) = F_e(\mathcal{S}_{\text{th}}^\dagger \mathcal{S}_{\text{op}}) , \quad (7)$$

where F_e is the entanglement fidelity defined by Schumacher [1]. Accordingly, we will refer to this quantity as the gate fidelity. It can be shown that this fidelity satisfies $\bar{C}_A(\rho_{\text{th}}, \rho_{\text{op}}) \geq C_A(\mathcal{S}_{\text{th}}, \mathcal{S}_{\text{op}})$, with equality if $\text{tr}(\rho_{\text{in}}^2) = \text{tr}(\rho_{\text{th}}^2)$ for all the input states [3].

Our analysis utilizes two different representations of quantum operations, the supermatrix representation and the Kraus operator sum representation. The supermatrix \mathcal{S} operates on the density matrix as

$$\text{col}(\rho_{\text{fin}}) = \mathcal{S} \text{col}(\rho_{\text{ini}}) , \quad (8)$$

where ρ_{ini} and ρ_{fin} are the initial and final density matrices, and the “col” operation stacks the columns of the density matrices on top of one another in left to right order. This results in an $N \times N$ matrix becoming a column vector of length N^2 . We will primarily work in two different supermatrix bases, the computational (or Zeeman) basis and the product operator basis. In the computational basis the rows and columns of the $2^n \times 2^n$ density matrix are labeled by the binary expansion of their indices from $|0 \dots 0\rangle$ to $|1 \dots 1\rangle$. The product operator basis is related to the structure of the NMR Hamiltonian and rows and columns of the supermatrix in this basis are labeled as $I_2 \otimes \dots \otimes I_2$, $I_2 \otimes \dots \otimes I_2 \otimes \sigma_x$, to $\sigma_z \otimes \dots \otimes \sigma_z$, where “ \otimes ” denotes tensor multiplication, the σ ’s are the standard Pauli matrices, I_2 is the 2×2 identity matrix and each term has n factors (see Ref. [23] for details).

The superoperator of a quantum operation can also be expressed as a Kraus operator sum. This sum is comprised of a set of $N \times N$ matrices, A_k , such that

$$\rho_{\text{fin}} = \sum_k A_k \rho_{\text{ini}} A_k^\dagger \quad (9)$$

where the sum may require as many as N^2 terms. It is easily seen that a Kraus operator sum preserves the Hermiticity of ρ_{ini} , and that it preserves the trace if and only if

$$\sum_k A_k^\dagger A_k = 1 . \quad (10)$$

If the operation is purely unitary there is only one Kraus operator, which is just the unitary operator in question. In general, however, there are an infinite number of equivalent Kraus operator representations of a given quantum operation. The least-squares fitting procedure described below yields a Kraus operator sum representation in which the Kraus operators are both mutually orthogonal, minimum in number and sorted by the size of the contribution each makes to ρ_{fin} .

III. INCOHERENT ERRORS

A superoperator is completely positive if it admits a Kraus operator sum representation. Although this condition holds for the physical processes usually studied in the quantum mechanics of open systems, including unitary operations and decoherence via weak interactions with a Markovian environment, it is not difficult to construct situations in which not only complete positivity, but even the distinction between a state and its transformations breaks down [24, 25, 26, 27]. Such situations can only arise when the initial state of the system is not pure, but can be represented by a probability distribution over an ensemble of pure states with density matrix ρ_{ini} . Suppose the ensemble's probability distribution depends on some classical parameter c (usually space or time) and that ρ_{ini} also represents an average over c (see below for a concrete example). Then if the applied transformation \mathcal{K} likewise depends on c , so that the transformation is *correlated* with the states in the ensemble, then the final density matrix ρ_{fin} will generally not be equal to the result of applying the average of \mathcal{K} over c to ρ_{ini} . Indeed there will usually be no superoperator which maps every possible ρ_{ini} to the correct ρ_{fin} . In principle one could define a non-linear transformation that produces this mapping, but this is not very useful in practice because the large amount of

information needed to define a general non-linear transformation is neither readily available nor easy to work with.

Incoherent errors are precisely those which depend upon some classical parameter that labels the members of an ensemble, and so generate a correlation between the states in the ensemble and this parameter. In the NMR experiments described below, the main source of incoherent errors is the spatial inhomogeneity in the RF (radio-frequency) field over the sample volume. This may be expressed by writing the Hamiltonian for the interaction of the spins with the RF field in the form

$$H_{\text{RF}}(t; \vec{r}) = \alpha(t) \gamma B_1(\vec{r}) e^{-i\Delta\omega t\sigma_z/2} \sigma_x e^{i\Delta\omega t\sigma_z/2}, \quad (11)$$

where $\alpha(t)$ is the envelope of the field, γ is the gyromagnetic ratio of the spins, $B_1(\vec{r})$ is the magnitude of the field at the point \vec{r} , $\Delta\omega$ is the difference between the frequency of the RF field and the resonance frequency of the spins in the static magnetic field B_0 , and the σ 's are the usual Pauli matrices. Thus, the unitary operation $U = \exp(\int dt H_{\text{RF}})$ depends upon the position \vec{r} in the sample as well as time, i.e. $U = U(t; \vec{r})$, as does the resulting spin state $\rho(t; \vec{r}) = U(t; \vec{r})\rho(0; \vec{r})U^\dagger(t; \vec{r})$. The equilibrium state of the spins in the static field B_0 is independent of \vec{r} over the sample volume, so we may take $\rho(0; \vec{r}) = \rho(0)$ to be constant. The density operator that is observed is the integral over the sample volume V , i.e.

$$\rho(t) = \int_V d\vec{r} \rho(t; \vec{r}) = \int_V d\vec{r} U(t; \vec{r})\rho(0)U^\dagger(t; \vec{r}) \equiv \mathcal{S}(t)\rho(0). \quad (12)$$

where $\mathcal{S}(t)$ denotes the net superoperator of the actual quantum operation implemented. We can express this in matrix form as [13]

$$\text{col}(\mathcal{S}(t)\rho(0)) = \left(\int_V d\vec{r} \overline{U}(t; \vec{r}) \otimes U(t; \vec{r}) \right) \text{col}(\rho(0)), \quad (13)$$

where \overline{U} is the complex conjugate of U and the “col” operator maps $N \times N$ matrices to (N^2) -dimensional column vectors, as described above.

Describing the evolution of an ensemble by integrating over its spatial degrees of freedom works well for a single operation. When a second operation \mathcal{S}_2 is applied following the first \mathcal{S}_1 , however, we must take the spatial correlations produced by the first into account in computing the correct overall superoperator. In terms of the foregoing equations, this may be expressed as

$$\mathcal{S}_2 \mathcal{S}_1 = \int_V d\vec{r}_2 \left(\overline{U}_2(\vec{r}_2) \otimes U_2(\vec{r}_2) \right) \int_V d\vec{r}_1 \left(\overline{U}_1(\vec{r}_1) \otimes U_1(\vec{r}_1) \right)$$

$$\begin{aligned}
&= \int_V d\vec{r}_2 \int_V d\vec{r}_1 \left(\overline{U}_2(\vec{r}_2) \overline{U}_1(\vec{r}_1) \right) \otimes \left(U_2(\vec{r}_2) U_1(\vec{r}_1) \right) \\
&\neq \int_V d\vec{r} \left(\overline{U}_2(\vec{r}) \overline{U}_1(\vec{r}) \right) \otimes \left(U_2(\vec{r}) U_1(\vec{r}) \right) = \mathcal{S},
\end{aligned} \tag{14}$$

where \mathcal{S} is the true superoperator of the combined operations. Clearly, a similar result could be obtained if we were integrating over time, although that is not relevant to the experiments described in this paper. A simulation of an example of the lack of composibility of superoperators describing incoherent errors is shown in Fig. 3.

It follows that the $N^2 \times N^2$ supermatrix produced by our QPT procedure (Fig. 2) cannot be expected to precisely correspond to any physical process, and it will usually even fail to define a completely positive and trace-preserving superoperator. In this event, an improved estimate of the supermatrix of the quantum process that is realized by the QFT implementation can be obtained by making the smallest possible change to the supermatrix derived from QPT so as to make it completely positive and trace-preserving (CPTP).

One can, of course, always convert a Kraus operator sum into an equivalent supermatrix via the “*col*” operation introduced above,

$$\text{col} \left(\sum_k A_k \rho_{\text{ini}} A_k^\dagger \right) = \left(\sum_k \overline{A}_k \otimes A_k \right) \text{col}(\rho_{\text{ini}}). \tag{15}$$

To go the other direction, i.e. to take a supermatrix \mathcal{S} and convert it into an equivalent Kraus operator sum, we first rearrange its elements into a Hermitian supermatrix called the Choi supermatrix [13],

$$\mathcal{T} = \sum_{ij=0}^{N-1} (E_{ij} \otimes I_N) \mathcal{S} (I_N \otimes E_{ij}), \tag{16}$$

where I_N is the $N \times N$ identity matrix and E_{ij} is a matrix of zeros except for a 1 in the (i, j) th position. Then, if $\mathcal{T} = \sum_k \lambda_k v_k v_k^\dagger$ is the spectral decomposition of \mathcal{T} and we assume that all the eigenvalues $\lambda_k \geq 0$, our Kraus operators A_k may be shown to be

$$\text{col}(A_k) = \sqrt{\lambda_k} v_k \quad (k = 1, \dots, N). \tag{17}$$

It follows from the above that a superoperator \mathcal{S} is completely positive if and only if its Choi supermatrix is positive semi-definite. In the event that an experimentally determined supermatrix \mathcal{S}_{obs} does not have a positive semi-definite Choi supermatrix, it has been shown [13] that the completely positive superoperator \mathcal{S}' closest to it in the least-squares sense may be obtained simply by setting the negative eigenvalues of its Choi supermatrix to zero to

get a new matrix \mathcal{T}' , and mapping it back to \mathcal{S}' via Eqn. (16) with \mathcal{S} and \mathcal{T} swapped. This procedure, however, will result in a supermatrix \mathcal{S}' that does not preserve the trace of the density matrix. That condition can be reimposed by subtracting

$$\Delta\mathcal{T}' \equiv N^{-1} \text{col}(I_N) \text{col}^\dagger(I_N) \mathcal{T}' - I_{N \times N} \quad (18)$$

from \mathcal{T}' , with the result that \mathcal{T}' is no longer positive semi-definite. It has further been shown, however, that iterating on these two procedures generates a sequence of supermatrices which converges to the Choi supermatrix corresponding to the superoperator that is closest to \mathcal{S} and is *both* trace preserving and completely positive. This is described for the experimental results in the Section VIII.

In order to quantify the extent to which a supermatrix violates the completely positive requirement, we define the positivity as the ratio of the sum of eigenvalues of the Choi matrix corresponding to the supermatrix over the sum of positive eigenvalues of the said Choi matrix. For a completely positive superoperator the positivity is equal to 1, while the presence of negative Choi eigenvalues causes the positivity to be less than 1.

IV. THE SPIN SYSTEM AND THE EXPERIMENTS

The experiments were implemented on a three-qubit NMR quantum information processor [28, 29]. The three qubits used were the three carbon spins in molecules of ^{13}C -enriched alanine in an aqueous solution. The internal Hamiltonian of this system has the form

$$H_s = \pi \sum_{i=1}^3 \nu_C^i \sigma_{C,z}^i + \frac{\pi}{2} \sum_{j>i=1}^3 J_{C,C}^{i,j} \vec{\sigma}_C^i \cdot \vec{\sigma}_C^j, \quad (19)$$

where ν_C^i are the Larmor frequencies of the spins and $J_{C,C}^{i,j}$ are the strengths of the couplings between them, both in frequency units. In our indexing scheme, a superscript 1 labels the carbonyl carbon of alanine, 2 the alpha carbon and 3 the methyl carbon. A separate time-dependent external Hamiltonian, shown in Eqn. (11), must be added whenever an RF pulse is applied to rotate qubits. In the 7 Tesla magnet used for the experiments, the resonant frequency of carbon-13 is approximately 75.468 MHz. Frequency changes, also known as chemical shifts, among the spins introduce differences $\nu_C^2 - \nu_C^1 = 9456.5$ Hz, $\nu_C^3 - \nu_C^2 = 2594.3$ Hz and $\nu_C^3 - \nu_C^1 = 12050.8$ Hz. The coupling constants between the three spins are $J_{C,C}^{1,2} = 54.2$ Hz, $J_{C,C}^{2,3} = 35.1$ Hz, and $J_{C,C}^{1,3} = -1.2$ Hz. In the absence of RF, the T_1 relaxation times

of the three spins are all longer than 1.5 s, while the T_2 relaxation times are longer than 400 ms (see Table I for exact numbers).

To rotate qubits we used the strongly modulating pulses introduced in Refs. [3, 10]. The first generation of strongly modulating pulses were designed to perform the desired propagator while refocussing the spins' known internal Hamiltonian [3]; the second generation was designed to also compensate for RF field inhomogeneity [10]. This was done by including the RF inhomogeneity profile in the simulations and, hence, in the target function minimized to design the compensated pulses. Pulses designed in this way performed near-optimally over the range of RF powers experienced by the ensemble of spins. While the simulated peak fidelities were lower than with the uncompensated pulses, the actual performance of the compensated pulses in the spectrometer was greatly enhanced.

The method of implementing the QFT via NMR is the same as in our previous QFT implementations [8, 22], with the added benefit of the RF pulses that compensated for RF-inhomogeneity. The pulse sequences for the Hadamard and conditional phase gates are derived from an idempotent or correlation operator description of the propagators [30]. The Hadamard gate pulse sequence is:

$$H_j = \left(\frac{\pi}{2}\right)_y^j - \left(\pi\right)_x^j. \quad (20)$$

This pulse program reads: apply a pulse that rotates spin j by 90° about the y-axis, followed by a pulse that rotates j by 180° about the x-axis. The B_{jk} gate, can be implemented using the coupling between qubits and the following pulse sequence:

$$\left(\pi\right)_\phi^j - \left(\frac{\theta_{jk}}{2\pi J_{jk}}\right) - \left(\pi\right)_\phi^j - \left(\frac{\pi}{2}\right)_y^{j,k} - \left(\frac{\theta}{2}\right)_x^{j,k} - \left(\frac{\pi}{2}\right)_{\bar{y}}^{j,k}. \quad (21)$$

where ϕ is an arbitrary phase. The notation $\left(\frac{\theta_{jk}}{2\pi J_{jk}}\right)$ represents a time interval during which $\sigma_z^j \sigma_z^k$ evolution occurs while chemical shifts and all other qubit couplings are refocused, while the superscript j, k denotes a pulse which rotates only spins j and k . The final three pulses in the above sequence perform a rotation around the z-axis. In our previous work [8] the bit reversal was implemented experimentally. Here the bit reversal is achieved by simply renaming the bits.

We stress that the various building blocks of the QFT implementation, i.e. the individual pulses and evolution periods, remain unchanged for all experiments. After creation of each initial state a fixed sequence is applied that is independent of the initial state.

The input states, $\{\rho_{\text{in}}\}$, used were the 64 product operator states (neglecting the large but undetectable identity component). These are 0 (actually the identity I_8), and states such as σ_x^1 , σ_z^3 , and $\sigma_y^2\sigma_x^3$ where the superscripts represent the spin indices, as above. These states were chosen because they are orthogonal and easy to create on a liquid-state NMR system. We order the states lexicographically starting with 0, followed by $\sigma_x^3 = I_2 \otimes I_2 \otimes \sigma_x$, $\sigma_x^2 = I_2 \otimes \sigma_x \otimes I_2$, and so on until $\sigma_z^1\sigma_z^2\sigma_z^3 = \sigma_z \otimes \sigma_z \otimes \sigma_z$ (the complete ordering may be found in Fig. 8). The QFT gate sequence described above is applied to each of these 64 states to obtain the corresponding set of output states $\{\rho_{\text{op}}\}$.

In any given three-spin spectrum only 24 of the 64 product operators are observable. Thus, to completely reconstruct the state of the system, each experiment is repeated 7 times with different readout pulses appended to the experiment. The real amplitudes of the peaks in the spectrum were then used as the coefficients of the product operators which were transformed into the corresponding observable product operators by the readout pulses. This procedure, known as state tomography [3], was done for all input and output states.

V. THE SYSTEM-PLUS-APPARATUS MODEL

Quantum process tomography serves experimentalists in two ways. First, it provides a thorough test of the model of the system-plus-apparatus used to design and interpret the experiments. Second, it provides a complete picture of the net effects of all the errors made in implementing the experiment and, in conjunction with the model, allows these effects to be unravelled into specific defects in the apparatus – and perhaps also the model. Before attempting this latter task, therefore, we wish to fully present, discuss, and justify the model we used for QPT on the QFT. This model includes the following attributes:

- The Hilbert space of the system in question and its Hamiltonian.
- The Hilbert space of the larger system with which the given system interacts coherently, and the Hamiltonian describing these interactions.
- The relaxation superoperator of the system, and some knowledge of how the larger system relaxes.
- Bounds on the precision of the classical control fields applied.

- The distribution of incoherent variations in these fields across the sample.

Both the fields and the positions of the spins can be treated classically. Since the larger system contains only a total of eight spins, we can simulate it exactly. Further information, for example the correlation times or full spectral densities of the noise generators driving relaxation [32], could have been included in the model, but the above proved adequate to explain most of the experimental observations for the QFT.

The first attribute is the Hamiltonian for the three carbon-13 spins of alanine used as qubits for the QFT, which has the form of H_s given in Eqn. (19). The larger system includes, in addition to the carbons, the four (nonexchanging) hydrogens and the spin-1 nitrogen-14 nucleus in alanine. The larger system's Hamiltonian has the form

$$\begin{aligned}
H_S = H_s + \pi \sum_{i=1}^4 \nu_H^i \sigma_{H,z}^i + \pi \nu_N \sigma_{N,z} + \frac{\pi}{2} \sum_{j>i=1}^4 J_{H,H}^{i,j} \vec{\sigma}_H^i \cdot \vec{\sigma}_H^j + \\
\frac{\pi}{2} \sum_{i=1}^4 \sum_{j=1}^3 J_{C,H}^{i,j} \sigma_{H,z}^i \sigma_{C,z}^j + \frac{\pi}{2} \sum_{i=1}^3 J_{N,C}^i \sigma_{N,z} \sigma_{C,z}^i + \frac{\pi}{2} \sum_{j=1}^4 J_{N,H}^j \sigma_{N,z} \sigma_{H,z}^j,
\end{aligned} \tag{22}$$

where we have used the well-known fact that couplings between spins with distinct gyromagnetic ratios can be truncated to just the secular (i.e. $\sigma_z \sigma_z$) part.

The spin-1 nitrogen has an electric quadrupole moment and hence a short T_1 , so its coupling to the other spins cannot be observed. As a result, the nitrogen can be omitted from the Hamiltonian, although it still plays a role in the relaxation of the other spins. The spin-lattice (T_1) relaxation time of the hydrogen atoms, on the other hand, is longer than the experiment, so here we must include the additional frequency shifts that depend upon their spin states. In other words, we take the $\sigma_{H,z}$ to be constants of the motion, and treat the carbons as an incoherent mixture of $2^4 = 16$ independent 3-spin systems, each with their resonance frequencies shifted by one of the 16 possible sums of $\pm J_{C,H}/2$. Because we start with the spins in the high-temperature equilibrium state, each of these 16 independent evolutions contributes equally to the simulated density matrix.

The computer search for the strongly modulating control sequences (pulses) is quite demanding, and it is important to keep the Hilbert space as small as possible during the associated simulations. For this reason the simulations described in this paper ignored the four hydrogen atoms in the alanine molecule, which were left aligned with the main magnetic field during the actual experiments but which nonetheless have couplings to the carbons on

the order of 150Hz. A better way, which we subsequently implemented and is described here for completeness, would be to average the results of 16 simulations over each of the 3-spin Hamiltonians

$$H_{s,c}^{\underline{\delta}} = \pi \sum_{i=1}^3 \left(\nu_C^i + \sum_{j=1}^4 \frac{(-1)^{\delta_j}}{2} J_{C,H}^{i,j} \right) \sigma_{C,z}^i + \pi \sum_{j>i=1}^3 J_{H,H}^{i,j} \vec{\sigma}_H^i \cdot \vec{\sigma}_H^j, \quad (23)$$

for all combinations of $\underline{\delta} \equiv [\delta_1, \dots, \delta_4] = \{0, 1\}^4$, where the “c” stands for “control”. This is much faster than diagonalizing the Hamiltonian with the four hydrogens included (16 times longer as opposed to $\sim 16^3$).

During the free evolution periods between pulses, on the other hand, we applied additional (hard) π -pulses to the carbons to refocus this unwanted phase evolution, in accord with the free-evolution Hamiltonian used for these (much less demanding) simulations,

$$H_{S,f} = H_s + \pi \sum_{i=1}^4 \sum_{j=1}^3 J_{C,H}^{i,j} \sigma_{H,z}^i \sigma_{C,z}^j, \quad (24)$$

where the “f” now stands for “free”. The frequency evolution of the hydrogens can be neglected because they are left along the z-axis, thereby also avoiding population disturbances that would lead to nuclear Overhauser cross-relaxation and thereby memory effects.

The search for strongly modulating control sequences was further simplified by assuming that the RF phase, amplitude, and frequency was piecewise constant, so the total unitary transformation was given by the product

$$U_{\text{tot}}^{\underline{\delta}} = \prod_{k=1}^{k_{\text{max}}} U_k^{\underline{\delta}} = \prod_{k=1}^{k_{\text{max}}} \text{T exp} \left(-i(t_k - t_{k-1}) H_{S,c}^{\underline{\delta}} - i \int_{t_{k-1}}^{t_k} dt H_{\text{RF},k}(t) \right) \quad (25)$$

Here, “T” denotes the usual time-ordering operator, and the external RF Hamiltonian during the k -th interval is given by

$$H_{\text{RF},k}(t) = \alpha_k \gamma_C B_1 \sum_{j=1}^3 \left(e^{-i(\pi t \nu_k + \phi_k)} \sigma_{C,z}^j \sigma_{C,x}^j e^{i(\pi t \nu_k + \phi_k)} \sigma_{C,z}^j \right), \quad (26)$$

where α_k is the relative amplitude of the field during the k th interval (cf. Eqn. 11). This assumption allows the unitaries $U_k^{\underline{\delta}}$ for each interval to be calculated exactly by transforming to an interaction frame in which $H_{\text{RF},k}$ becomes time-independent, and diagonalizing the net Hamiltonian in that frame [3]. The spectrometer generates the control fields by applying a time-dependent voltage to a tuned resonator. The limitations on both the control circuitry

and the tuned resonator introduce time-dependent distortions of this modulation at the discontinuities between intervals. To account for this limitation, we monitor the field generated in the control coil (the antenna that interacts with the spins) and pre-weight the time dependent wave-form to provide a close approximation to the desired shape. In addition, we use the measured modulation sequence in the simulator to follow the dependence of the propagator for small distortions.

To achieve useable sensitivity, NMR is carried out on an ensemble of spatially distributed spins. The control field thus varies over the spatial extent of the sample, which is termed RF field inhomogeneity. This variation could be reduced by using a larger coil, a smaller sample, or by selecting a particularly homogeneous region of the sample via a magnetic field gradient. All of these options, however, reduce the signal-to-noise ratio. Fortunately, the spatial variation of the RF field is constant over time, and can be measured very accurately. This allows us to perform the simulations for each member of a histogram of the variations in RF amplitude across the sample, and to combine the results as an incoherent sum just as was described for the variations in the hydrogen spin states above. A total of 33 values was included in this RF inhomogeneity histogram (see Fig. 4).

The procedure used to find a modulation sequence that correctly implements any desired unitary operation seeks to maximize the fidelity between the desired unitary superoperator $\bar{U}_{\text{th}} \otimes U_{\text{th}}$ and the simulated superoperator \mathcal{S}_{op} . The latter was obtained as an incoherent or Kraus operator over the 33 RF field strengths in the experimentally measured RF inhomogeneity histogram, i.e.

$$\mathcal{S}_{\text{op}}(\rho) = \sum_{\ell=1}^{33} p_{\ell} U_{\ell} \rho U_{\ell}^{\dagger} \equiv \sum_{\ell=1}^{33} A_{\ell} \rho A_{\ell}^{\dagger}. \quad (27)$$

Thus, the gate fidelity as defined in Eqn. (7) can be calculated directly from the Kraus operators A_m as

$$\begin{aligned} F_{\text{e}}((\bar{U}_{\text{th}} \otimes U_{\text{th}})^{\dagger} \mathcal{S}_{\text{op}}) &\equiv \frac{\text{tr}((\bar{U}_{\text{th}} \otimes U_{\text{th}})^{\dagger} \mathcal{S}_{\text{op}})}{\text{tr}((\bar{U}_{\text{th}}^{\dagger} \bar{U}_{\text{th}}) \otimes (U_{\text{th}}^{\dagger} U_{\text{th}}))} = \frac{1}{64} \sum_{m=1}^{33} \text{tr}((\bar{U}_{\text{th}} \otimes U_{\text{th}})^{\dagger} (\bar{A}_m \otimes A_m)) \quad (28) \\ &= \frac{1}{64} \sum_{m=1}^{33} \text{tr}((\bar{U}_{\text{th}}^{\dagger} \bar{A}_m) \otimes (U_{\text{th}}^{\dagger} A_m)) = \frac{1}{64} \sum_{m=1}^{33} |\text{tr}(U_{\text{th}}^{\dagger} A_m)|^2. \end{aligned}$$

In simulations including the four hydrogen spins, the sum on the right-hand side of this formula must be increased by another factor of 16 in taking the partial trace over the hydrogen spins.

TABLE I:

Measured carbon-13 decay rates for each type of product operator (s^{-1}) in the alanine molecule used for the experiments. These include the inverses of the relaxation times T_1 and T_2 for all three carbon-13 spins. The “x|y” subscripts indicate that, in every operator of the corresponding product, all the labels to the left or to the right of the bar must be used together, thus indicating a total of two products with one expression.

Type of Product Operator	Decay Rate	Type of Product Operator	Decay Rate
σ_z^1	0.032 ± 0.01	σ_z^2	0.345 ± 0.01
σ_z^3	0.583 ± 0.01	$\sigma_z^1 \sigma_z^2$	0.282 ± 0.01
$\sigma_z^1 \sigma_z^3$	0.458 ± 0.01	$\sigma_z^2 \sigma_z^3$	0.689 ± 0.01
$\sigma_z^1 \sigma_z^2 \sigma_z^3$	0.684 ± 0.01	$\sigma_{x y}^1, \sigma_{x y}^1 \sigma_z^2,$ $\sigma_{x y}^1 \sigma_z^3, \sigma_{x y}^1 \sigma_z^2 \sigma_z^3$	1.89 ± 0.02
$\sigma_{x y}^2, \sigma_z^1 \sigma_{x y}^2,$ $\sigma_{x y}^2 \sigma_z^3, \sigma_z^1 \sigma_{x y}^2 \sigma_z^3$	3.19 ± 0.01	$\sigma_{x y}^3, \sigma_z^1 \sigma_{x y}^3,$ $\sigma_z^2 \sigma_{x y}^3, \sigma_z^2 \sigma_z^1 \sigma_{x y}^3$	1.68 ± 0.01
$\sigma_{x y}^1 \sigma_{y x}^2, \sigma_{x y}^1 \sigma_{y x}^2 \sigma_z^3,$ $\sigma_{x y}^1 \sigma_{x y}^2, \sigma_{x y}^1 \sigma_{x y}^2 \sigma_z^3$	6.93 ± 0.11	$\sigma_{x y}^1 \sigma_{y x}^3, \sigma_{x y}^1 \sigma_z^2 \sigma_{y x}^3,$ $\sigma_{x y}^1 \sigma_{x y}^3, \sigma_{x y}^1 \sigma_z^2 \sigma_{x y}^3$	3.56 ± 0.06
$\sigma_{x y}^2 \sigma_{y x}^3, \sigma_z^1 \sigma_{x y}^2 \sigma_{y x}^3,$ $\sigma_{x y}^2 \sigma_{x y}^3, \sigma_z^1 \sigma_{x y}^2 \sigma_{x y}^3$	6.81 ± 0.10	$\sigma_{y x}^1 \sigma_{x y}^2 \sigma_{x y}^3, \sigma_{x y}^1 \sigma_{y x}^2 \sigma_{x y}^3,$ $\sigma_{x y}^1 \sigma_{x y}^2 \sigma_{y x}^3$	13.48 ± 0.81
$\sigma_{x y}^1 \sigma_{x y}^2 \sigma_{x y}^3$	14.58 ± 0.20		

The relaxation superoperator for the carbons in alanine was measured in the absence of RF fields, and found to have 98.5% of its norm along the diagonal in the product operator basis. This means that the various product operator components decay mono-exponentially, without cross-relaxation, so that it can be described by an 8×8 “Hadamard relaxation matrix” [23, 31]. This is shown pictorially in Fig. 5, while precise values for the various types of rates seen in the figure are given in Table I.

To be complete, the relaxation superoperator should also be measured as a function of the applied RF fields (and include memory effects due to nuclear Overhauser effects with the hydrogens [32]). The QFT, however, efficiently mixes the states of the three carbon spins, so that on average over its implementation the decoherence is indistinguishable from a uniform, isotropic attenuation of all the product operator components. That is to say, QFT on the QFT is not able to provide any details regarding the physical relaxation

processes operative in alanine, save for an average overall rate of attenuation. Of course, QPT could be performed on a simpler gate, as in Ref. [15] where it was used to derive a relaxation superoperator for free precession, but the goal here is to use QPT to learn about the coherent and incoherent errors committed during implementation of a complex unitary transformation, the QFT. Therefore, this simple effective relaxation superoperator was assumed to accelerate the simulations of the overall QFT (no relaxation was assumed during the pulse design simulations, since they are not intended to correct for such effects).

VI. AN OVERVIEW OF THE EXPERIMENTAL RESULTS

Complete QPT was performed twice using different sets of strongly modulating RF control sequences to implement single spin rotations (Section IV). The first such iteration was done with the sequences described in Ref. [3], which refocussed the evolution under the alanine molecule’s internal spin Hamiltonian (H_s in Eqn. 19) during the sequence. The second iteration used control sequences that not only refocussed the internal Hamiltonian, but also compensated for inhomogeneity in the RF field itself [10]. Thus, the second set of control sequences was expected to produce much smaller incoherent errors than the first, while the coherent and decoherent errors were expected to be roughly the same for both. The improvement obtained with the RF-compensated set is illustrated in Fig. 6, which plots the correlations and attenuated correlations obtained for each of the 64 product operator basis states used as inputs for the two iterations against one another. Further evidence for substantial improvements with the RF-compensated control sequences may be obtained from the Kraus operator plots and statistics in Fig. 7 (see below for their interpretation). Having demonstrated this clear-cut improvement, all subsequent analysis will be given only for the results obtained with the compensated control pulses.

The correlation provides an estimate of the accuracy of the experimental QFT implementation, but without considering the loss of magnetization due to decoherence or incoherence. The average of the input state correlations over all 64 basis states was 0.96, while the average correlation following application of the QFT was 0.82. A minimization search, however, found pure states which, after operating on them with the experimental superoperator, had a correlation with the same pure state following the theoretical QFT as low as 0.45. The average attenuated correlation (or gate fidelity [3]), which also takes into account the loss of

magnetization, was 0.64, indicating that about 22% of the magnetization was lost over the ca. 30 ms needed to implement the QFT (see Section IV). These numbers are in-line with expectations based on other recent applications of the RF-compensated control sequences [4]. About half of this magnetization loss was expected due to intrinsic decoherence, and since approximately the same amount of decoherence occurred during the input states' read-out as during the output states', the remainder is probably due to residual uncompensated incoherence and/or imperfect decoupling of the protons from the carbons used as qubits. These issues will be discussed in more detail in later sections. A complete list of all the output state (attenuated) correlations may be found in Fig. 8 below.

Rather than looking at the action of the QFT on states, one can also look directly at the Kraus operator sum computed from the completely positive part of the experimental supermatrix \mathcal{M}_{obs} (Section III). Each Kraus operator A_k has an associated amplitude, $a_k = \|A_k\|/\sqrt{8} = \sqrt{\lambda_k/8}$ (where λ_k is the k th eigenvalue of the associated Choi supermatrix), and since in a perfect implementation the desired unitary operator U_{QFT} would be the only Kraus operator with nonzero amplitude, one expects the Kraus operator with the largest amplitude to be at least fairly similar to U_{QFT} . This is confirmed by the plots of the real part of the largest Kraus operator, shown in Fig. 7, which had an amplitude $a_1 = 0.86$ and a correlation with the real part U_{QFT} of 0.95, implying a net coherent error of roughly 5%. The second largest Kraus operator, also shown, had an amplitude of $a_2 = 0.34$, and was also rather close to unitary although uncorrelated with U_{QFT} . We expect it to be a rough approximation to the largest unitary operator in any sum of unitary transformations making up the incoherent error. Finally, there are another 32 essentially non-unitary Kraus operators in the completely positive part of the experimental QFT supermatrix with smaller amplitudes (Fig. 7).

The non-completely positive part of the QFT supermatrix, which is obtained from the eigenvectors associated with the negative eigenvalues of its Choi supermatrix, will also be of interest in what follows. The positivity of the QFT supermatrix, as defined at the end of Section III, was only 0.60, but the ratio of the smallest to the largest Choi supermatrix eigenvalues was -0.075 , indicating that the negative eigenvalues were rather small in magnitude in comparison to the positive. The ratio with the second largest was -0.48 , and the third had almost the same magnitude as the smallest. These observations, together with the well-known sensitivity of the eigenvectors of nearly degenerate eigenvalues to small

perturbations in the elements of the matrix from which they come, imply that rather little information about the errors made in the QFT implementation can be gleaned from the individual Kraus operators after the first two. Only the subspaces spanned by the eigenvectors associated with all of the smaller positive, or perhaps negative, eigenvalues is likely to be statistically significant.

VII. COMPARISON WITH THE MODEL

To assess the precision and completeness of our system-plus-apparatus model, the complete set of experiments involved in QPT on the QFT was simulated using the mathematical model of the system-plus-apparatus described in Section V. The compatibility of the simulated results with the experimental provides a rigorous test for the accuracy of the model, which takes all the known significant imperfections of the experimental apparatus into account. All of the unitary operations performed during these simulations were implemented using exactly the same strongly modulating control sequences that were used for the experiments, and complete state tomography was performed for each input and output state. It should be noted, however, that these states were reconstructed directly from the observables in the simulated density matrices, without further simulating the spectra and fitting them as required in experimental state tomography (which of course gives rise to additional errors in the actual experiments). Figure 8 shows the correlation and attenuated correlation of the initial and final states obtained from these simulations.

Figure 9 plots the sorted Kraus operator amplitudes obtained from the simulated supermatrix, along with those from the experimental supermatrix for comparison (cf. Fig. 7). The negative values plotted are actually the negative square roots of the corresponding Choi matrix eigenvalues, and are shown to illustrate that the experimental supermatrix was significantly further from being completely positive than was the simulated (the positivity of the simulated was 0.86, as opposed to 0.60 for the experimental). The most likely reason for this is the absence in the simulations of the additional errors expected from fitting the spectra to extract the product operator amplitudes for state tomography. Also shown once again is the real part of the theoretical QFT unitary matrix (cf. Fig. 7), along with the real parts of the matrices of the largest Kraus operators from the experimental and simulated supermatrices. Finally, the corresponding best unitary approximations to the largest Kraus

operators, obtained by setting their singular values to unity, have their real parts shown on the bottom right-hand side of Fig. 9. It may be seen that there is a good correspondence between the largest Kraus operators as well as between their best unitary approximations, with a correlation between the simulation and the experiment of 0.90 in both cases. As noted previously, the smaller Kraus operators cannot be expected to correspond significantly to one another.

Since the Fourier transformation converts between the position and momentum bases, it has a very simple interpretation in phase space. Classically, a Fourier transform rotates phase space by 90° . In quantum phase space, the QFT superoperator has only one nonzero element equal to unity in each row and column, and so constitutes a permutation matrix [33]. This is shown in Fig. 10, along with the corresponding plots for the simulated and experimental supermatrices. One can see immediately from these plots that there are errors in the QFT implementation. The phase space basis, however, consists of operators that are neither Hermitian nor products of any underlying Hilbert space basis, and which are not related in any simple way to the physical operators used to implement the QFT. Thus, although the action of the QFT is very easy to understand in the phase space basis, it is very hard to interpret the discrepancies between the theoretical superoperator and observed supermatrix in terms of implementation errors in this basis. It is worth noting, nonetheless, that in the phase space basis the errors appear more white than Gaussian especially in the simulation.

Other bases, in which the discrepancies between the simulated and experimental supermatrices are also clearly manifested, include the computational basis (or Zeeman basis; see Fig. 11), and the product operator basis (shown in Fig. 12), where the latter consists of all possible products of the Pauli matrices σ_x , σ_y and σ_z of different spins [32] (see Section II above). It may be observed that the theoretical superoperator contains several fixed points in the product operator basis, which provide us with another interesting metric for the precision of our implementation. Two of these fixed points are $\sigma_x^1 \sigma_z^3$ and $(\sigma_x^1 + \sigma_z^3)/2$. The correlations between these fixed points, before and after applying the experimental and simulated superoperators, are 0.91 and 0.93 respectively. Further information can be obtained from plots of the individual rows, which depict how much each input state contributes to a given output state, as shown in the relatively simple case of the $\sigma_x^1 \sigma_z^3$ fixed point in Fig. 14.

The greatest part of the deviation between the simulated and experimental results is

expected to be due to the propagation of small coherent errors. Thus it is interesting to compare the simulated and experimental supermatrices after correcting for these errors as completely as possible. This is most simply done by left-multiplying by the inverse of the superoperator obtained from the best unitary approximation to the largest Kraus operator, $\overline{U}_1^\dagger \otimes U_1^\dagger$, followed by the theoretical unitary superoperator $\overline{U}_{\text{QFT}} \otimes U_{\text{QFT}}$, i.e.

$$\mathcal{M}_{\text{cor,obs|sim}} = (\overline{U}_{\text{QFT}} \otimes U_{\text{QFT}})(\overline{U}_{1,\text{obs|sim}} \otimes U_{1,\text{obs|sim}})^\dagger \mathcal{M}_{\text{obs|sim}} . \quad (29)$$

The resulting supermatrices in the phase space basis are displayed in Fig. 13, along with the exact QFT supermatrix in the same basis for comparison. It may immediately be seen that there has been a considerable improvement in the similarity of these matrices, as is further confirmed by a correlation between the corrected simulated and corrected experimental supermatrices of 0.94, between the corrected simulated and theoretical of 0.99, and between the corrected experimental and theoretical of 0.95. The correlations between the simulated and experimental correction factors, i.e. the products of the unitary superoperators in the above equation, are however only 0.90, indicating that the cumulative effects of coherent errors that were not taken into account by the simulations over the course of the experiments was roughly 10%. It should further be noted that whereas the experimental supermatrix is significantly more strongly correlated with the theoretical than it is with the simulated, after they have been corrected their correlations and attenuated correlations with the theoretical are very nearly the same.

VIII. DISCUSSION

We have shown that our model of the system-plus-apparatus is able to predict many details of the experimental results (see Table II for all the correlations among the theoretical, simulated and experimental supermatrices, together with the attenuated correlations to the theoretical). Specifically, simulations based on the Hadamard relaxation operator shown in Fig. 5 and Table I have allowed us to establish that the results contain no specific information on the decoherence rates and processes operative in our system, since these are averaged by the complex sequence of transformations that make up the QFT. Their net effect can therefore be modeled as a simple uniform attenuation of all the product operators in the density matrix other than the identity. This is explicitly demonstrated by the close

TABLE II:

The correlation coefficients between all pairs of supermatrices, labelled as described in the main text, together with the attenuated correlations (as defined in section II) between each and the theoretically exact supermatrix of the quantum Fourier transform.

Supermatrix	Correlations Among All Pairs of Supermatrices					Attenuated Correlation
Theoretical	1.00	0.89	0.99	0.82	0.95	1.00
Simulated	–	1.00	0.90	0.79	0.85	0.68
Corrected Sim.	–	–	1.00	0.81	0.94	0.76
Experimental	–	–	–	1.00	0.87	0.64
Corrected Exp.	–	–	–	–	1.00	0.74

correspondence between the supermatrix eigenvalues shown in Fig. 15, both from simulations using the Hadamard relaxation operator (red “*”) as well as from simulations taking no account of relaxation save by scaling down the nonidentity components of the density operators by a factor of 0.82 (blue “o”). In general, of course, relaxation cannot be accounted for by a single attenuation factor, and in fact methods similar to those described here have been used to determine the complete NMR relaxation superoperator of a two-spin system [15].

Figure 15 also shows the eigenvalues of the supermatrix obtained from simulations which included incoherent errors from RF field inhomogeneity, first without taking relaxation or readout errors into account (cyan “●”), and second from simulations which included input and output state readout and took relaxation into account by scaling the nonidentity components of the density matrices read out by 0.82 (green “×”). These plots show rather clearly that most of the additional dispersion seen in the simulations including incoherent errors stems directly from those errors, and was not an unintended consequence of the additional errors made during the readout operations needed for QPT (recall that incoherent errors were included in simulating the readout operations).

Nevertheless, the spread in the eigenvalues of the experimental superoperator (see Fig. 17 below) were significantly larger than those in the simulations of the full QPT procedure, and it was not possible to match them in a one-to-one fashion. In part this may be due to systematic errors in the least-squares fitting procedure by which the observables (m_{xx}

in Fig. 2) were extracted from the NMR spectra, in particular errors in distinguishing the absorptive and dispersive peak components. Such errors are difficult to simulate accurately and therefore not included in our simulations of the full QFT procedure, but are consistent with the fact that the largest single-spin corrections were z-rotations (as described below). Another, probably more important reason for these apparent discrepancies between the model and the experiments lies in the propagation of many small coherent errors over the course of the QFT implementation.

Even though the simulated single-qubit gate fidelities were all better than 0.99, they were also less than unity. The main thing that limited these fidelities was that the number of parameters, and hence the number of time intervals within which the RF amplitude and phase was held constant, had to be kept as low as possible during the optimizations by which the strongly modulating pulses were designed. Although the cumulative effects of such small errors could become significant, since they are included in the simulations they are not likely to be the source of the additional eigenvalue dispersion that is seen in the experimental results. A more important source of coherent errors is expected to be due to the fact that the protons were not included in any of the simulations, and their couplings to the carbons used as qubits will show up as phase rotations. In addition, the model ignores such fine details of the apparatus as the limits on the rise-and-fall times of the transmitter used to generate the RF control sequences, and more generally its frequency response characteristics. Although the simulation of reactive circuits is more complex than the simulation of resistive circuits, in due course we will also include such effects in the model, and continue to refine it until the only remaining discrepancies between the simulated and experimental results lie in the intrinsic measurement errors.

Unwanted bilinear interactions are refocussed during the QFT implementation by the application of π -rotations to the individual spins, using traditional NMR methods [32]. Errors in these rotations will contribute to the bilinear errors only to second order, so these bilinear errors depend mainly upon the timing of the pulses, which can be controlled very accurately. As a consequence, we expect that the residual coherent errors that were not taken into account by the simulations will be primarily single-spin rotations. To test this hypothesis, the error operator $U_{\Delta} = U_{1,\text{exp}} U_{1,\text{sim}}^{\dagger}$ was taken, where $U_{1,\text{exp}}$ is the best unitary approximation to the largest Kraus operator A_1 of the experimental supermatrix (cf. Fig. 9), and $U_{1,\text{sim}}$ is similarly the best unitary approximation to the largest Kraus operator of the

simulated supermatrix. Using a numerical search, the product of three single-spin rotations was found that fit U_Δ best in the least squares sense. The resulting unitary $U_\Delta^1 \otimes U_\Delta^2 \otimes U_\Delta^3$ had a correlation coefficient with U_Δ of 0.96, in support of the hypothesis.

The angles and directional cosines of the axes of these three rotations are shown in Table III, while the eigenvalues of the resulting corrected superoperators are shown in Fig. 16. It should be noted that, although the correlation between $U_{1,\text{exp}}$ and $U_{1,\text{sim}}$ increased from 0.90 to 0.96 on left-multiplying U_1 by the Hermitian conjugate of this product of single-spin rotation operators, these rotations are the cumulative result of many small rotation errors and are not simply traced back to any single short-coming in the experiments. For completeness, the axes and angles of the single-spin rotations that best fit the error operator $U_\Delta = U_{1,\text{sim}}^\dagger U_{1,\text{exp}}$ are also shown in Table III, together with the eigenvalues of the corresponding corrected superoperators in Fig. 16. The product of these rotations similarly has a 0.97 correlation with U_Δ , but in this case one must right-multiply $U_{1,\text{exp}}$ by the Hermitian conjugate of the product to correct it. The close co-incidence between the angles of rotation about the x-axis on spin 1 in the first case and about the z-axis on spin 3 in the latter case is expected, since $U_{\text{QFT}}\sigma_x^1 U_{\text{QFT}}^\dagger = \sigma_z^3$ (recall $\sigma_x^1 \sigma_z^3$ is a fixed point of the QFT).

Finally, it is of interest to demonstrate that despite a substantial number of negative eigenvalues in the Choi matrix of the experimental supermatrix, it is not necessary to change

TABLE III:

The two triples of single-spin rotations that optimize the correlation coefficient between the best unitary approximations to the largest Kraus operators of the experimental and simulated supermatrices, when the experimental supermatrix is left or right multiplied by the unitary matrix corresponding to each one of these triples.

Side	Spin	x, y & z-Directional Cosines of Rotation Axis			Rotation Angle
left	1	-0.992	0.007	0.123	36.7°
left	2	-0.386	-0.243	0.890	9.0°
left	3	0.703	0.701	-0.123	16.9°
right	1	0.059	-0.031	0.998	14.2°
right	2	0.227	-0.512	0.829	10.2°
right	3	-0.092	-0.292	-0.952	38.3°

it much in order to obtain a supermatrix which represents a completely positive and trace-preserving superoperator. For this reason the supermatrix $\mathcal{M}_{\text{CPTP}}$ which best-fit the Choi matrix of the experimental supermatrix subject to the constraint that it was both positive semidefinite and satisfied the trace-preservation conditions was computed as described in Section III. Although this procedure made essentially no change in the largest Kraus operator (as expected), it did have a significant effect on the experimental supermatrix as a whole. The correlations between this CPTP-fit and the other supermatrices that we have dealt with up to now are given in Table IV, along with those to the original experimental supermatrix for comparison. This shows that even though imposing the complete positivity constraint on the experimental observations did not change the supermatrix very much, the change was distinctly in the right direction since it improved the correlation with both the simulated and theoretical supermatrices. This is further confirmed by Fig. 17, which shows the eigenvalues of $\mathcal{M}_{\text{CPTP}}$, along with those of the superoperator $\bar{U}_{1,\text{CPTP}} \otimes U_{1,\text{CPTP}}$ obtained from the best unitary approximation to its largest Kraus operator (scaled down so as to have the same trace as $\mathcal{M}_{\text{CPTP}}$), and those of the experimental supermatrix \mathcal{M}_{obs} for comparison. From this we see that the eigenvalues of $\mathcal{M}_{\text{CPTP}}$ are closer to being cocircular, indicating that it is closer to an attenuated unitary than was \mathcal{M}_{obs} , but that only after taking the unitary part did they become perfectly cocircular.

TABLE IV:

The correlation coefficients between Theoretical, Simulated and Experimental supermatrices (see text) and the optimum completely positive and trace-preserving approximation $\mathcal{M}_{\text{CPTP}}$ to the experimentally determined supermatrix \mathcal{M}_{obs} , as well as the best unitary approximation to its largest Kraus operator $\bar{U}_{1,\text{CPTP}} \otimes U_{1,\text{CPTP}}$ and \mathcal{M}_{obs} itself for comparison.

Supermatrix	Correlation with $\bar{U}_{1,\text{CPTP}} \otimes U_{1,\text{CPTP}}$	Correlation with $\mathcal{M}_{\text{CPTP}}$	Correlation with \mathcal{M}_{obs}
Theoretical	0.86	0.89	0.82
Simulated	0.82	0.82	0.79
Experimental	0.95	0.97	1.00

IX. CONCLUSIONS

In conclusion, we have implemented quantum process tomography of the quantum Fourier transform on a three-qubit NMR quantum information processor. The overall gate fidelity (attenuated correlation between superoperator matrices) was 0.64, whereas the (unattenuated) supermatrix correlation was 0.82 (see Table II). Judging by the fact that making the unitary part of the largest Kraus operator correspond as closely as possible to the theoretical QFT gave a correlation of 0.95, we conclude that the loss of fidelity due to incoherence and/or measurement errors during state tomography was of order 5%. The loss of magnetization due to incoherence and decoherence, on the other hand, was $0.64/0.82 = 0.78$, i.e. about 22%. This implies that the cumulative effects of coherent errors reduced the fidelity by about $0.82/0.95 = 0.86$, or 14%, consistent with the fact that the correlation between the largest Kraus operator and the theoretical QFT unitary was $0.925 \approx \sqrt{0.86}$.

More importantly, QPT of the QFT has enabled us to validate the essential correctness of our model of the system-plus-apparatus used for the experiments in great detail, and to isolate its remaining shortcomings. It has further prompted us to develop a range of data analysis and visualization techniques for quantum process tomography, which should be broadly applicable in quantum information processing. The experiments described here demonstrate the precision with which complex quantum dynamics can be controlled, and highlights the significance of liquid-state NMR as a test bed for achieving such control. While full QPT on larger quantum systems will never be practical, the analysis done here should serve as an initial guide as to how information about the errors in quantum information processors can be extracted, and perhaps someday, how to debug a quantum computer.

ACKNOWLEDGEMENTS

The authors thank J.P. Paz for helpful discussions. This work was supported by ARDA/ARO grants DAAD19-01-1-0519 & DAAD19-01-1-0654, DARPA grant MDA972-01-1-0003, NSF grant EEC 0085557, the Air Force Office of Sponsored Research, and by the Cambridge-MIT Institute, Ltd.

- [1] B. Schumacher, Phys. Rev. A, **54**, 2614, (1996).
- [2] G. Teklemariam, E. M. Fortunato, M. A. Pravia, T. F. Havel, and D. G. Cory, Phys. Rev. Lett. **86**, 5845 (2001).
- [3] E. M. Fortunato, M. A. Pravia, N. Boulant, G. Teklemariam, T. F. Havel, D. G. Cory, J. Chem. Phys. **116**, 7599-7606, (2002).
- [4] N. Boulant, K. Edmonds, J. Yang, M. A. Pravia, and D. G. Cory, Phys. Rev. A **68**, 032305 (2003).
- [5] I. L. Chuang, M. A. Nielsen, J. Mod. Optics **44**, 2455 (1997).
- [6] J. F. Poyatos, J. I. Cirac, P. Zoller, Phys. Rev. Lett. **78**, 390 (1997).
- [7] G. M. D'Ariano, L. Maccone, Phys. Rev. Lett. **80**, 5465 (1998); G. M. D'Ariano, M. G. A. Paris, M. F. Sacchi, *Advances in Imaging and Electron Physics* (Academic Press, Englewood Cliffs, NJ), in press, <http://arxiv.org/abs/quant-ph/0302028>.
- [8] Y. S. Weinstein, M. A. Pravia, E. M. Fortunato, S. Lloyd, D. G. Cory, Phys. Rev. Lett. **86**, 1889 (2001).
- [9] M. H. Levitt, R. Freeman, J. Magn. Reson. **33**, 473 (1979); M. Levitt, J. Magn. Reson. **48**, 234 (1982); R. Tycko, Phys. Rev. Lett. **51**, 775 (1983); A. Shaka, R. Freeman, J. Magn. Reson., **55**, 487 (1983); M. Levitt, Prog. Nucl. Magn. Reson. Spect., **18**, 61 (1986).
- [10] M. A. Pravia, N. Boulant, J. Emerson, A. Farid, E. M. Fortunato, T. F. Havel, R. Martinez, D. G. Cory, J. Chem. Phys. **119**, 9003 (2003).
- [11] K. Kraus, *States, Effects, and Operations* (Springer-Verlag, Berlin, FRG, 1983).
- [12] D. W. Leung, J. Math. Phys. **44**, 528 (2003).
- [13] T. F. Havel, J. Math. Phys. **44**, 534 (2003).
- [14] A. M. Childs, I. L. Chuang, D. W. Leung, Phys. Rev. A **64**, 012314, (2001).
- [15] N. Boulant, T. F. Havel, M. A. Pravia, D. G. Cory, Phys. Rev. A **67**, 042322 (2003).

- [16] P. W. Shor, Siam. J. Comput. **26** 1484-1509 (1997).
- [17] R. Jozsa, Proc. Roy. Soc. Lond. **454** (1998).
- [18] C. Zalka, Proc. Roy. Soc. Lond. A **454** 313-322, (1998); S. Wiesner, quant-ph/9603028.
- [19] R. Schack, Phys. Rev. A **57** (1998).
- [20] D. Coppersmith, IBM Research Report RC19642 (1994).
- [21] M. D. Price, T. F. Havel and D. G. Cory, New J. Phys. **2**, 10 (2000).
- [22] Y. S. Weinstein, S. Lloyd, J. Emerson, D. G. Cory, Phys. Rev. Lett. **89**, 157902 (2002).
- [23] T.F. Havel, Quant. Inf. Proc., **1**, 511, (2003).
- [24] P. Pechukas, Phys. Rev. Lett. **73**, 8, (1994).
- [25] P. Stelmachovic, B. Buzek, Phys. Rev. A **64**, 062106, (2001).
- [26] P. Stelmachovic, B. Buzek, Phys. Rev. A **67**, 029902, (2003).
- [27] N. Boulant, S. Furuta, J. Emerson, T. F. Havel, D. G. Cory, quant-ph/0312116.
- [28] D. G. Cory, R. Laflamme, E. Knill, L. Viola, T. F. Havel, N. Boulant, G. Boutis, E. Fortunato, S. Lloyd, R. Martinez, C. Negrevergne, M. Pravia, Y. Sharf, G. Teklemarian, Y. S. Weinstein, Z. H. Zurek, Fortsch. Phys. **48**, 875 (2000).
- [29] J. A. Jones, Fortsch. Phys. **48**, 325 (2001).
- [30] S. S. Somaroo, D. G. Cory, T. F. Havel, Phys. Lett. A, **240**, (1998).
- [31] T.F. Havel, Y. Sharf, L. Viola, D.G. Cory, Phys. Lett. A, **280**, 282 (2001).
- [32] R. R. Ernst, G. Bodenhausen, A. Wokaun, *Principles of Nuclear Magnetic Resonance in One and Two Dimensions*, Oxford Univ. Press, Oxford (1994).
- [33] C. Miquel, J.P. Paz, M. Saraceno, Phys. Rev. A, **65**, 062309, (2002).

FIGURE CAPTIONS

FIG. 1: Circuit diagram for implementation of the quantum Fourier transform for three qubits. For each qubit j , starting with the most significant, a series of conditional phase gates are implemented between qubit j and all qubits more significant than j , followed by a Hadamard (H) on j . The amount of phase added is $\theta_{jk} = \pi/2^{j-k}$. A bit reversal (two-headed arrow) completes the QFT.

FIG. 2: A schematic of the QPT implementation used in this paper, together with two equations describing how the readout operations \mathcal{U}_{ro} and measurements m_{xx} ($\text{xx} = \text{in}, \text{op}$) are obtained from the ensemble of quantum systems described by the density matrix ρ ($\sigma_- \equiv \frac{1}{2}(\sigma_x - i\sigma_y)$). A set $\{\mathcal{S}_{\text{in}}\}$ of (not necessarily unitary) operations is performed, each in a separate experiment, on the equilibrium state ρ_{eq} of the spin system to create a complete set $\{\rho_{\text{in}}\}$ of input states. Each input state is then determined by quantum state tomography, i.e. by repetition of the experiment with different readout pulses, $\{\mathcal{U}_{\text{ro}}\}$, appended to each repetition. The readout pulses rotate unobservable components of the density matrix into observable components, the mean values $\{m_{\text{in}}\}$ of which are equal to the unobservables' mean values before rotation. Measurement of these mean values thus allows for the reconstruction of the input state that was actually created. Next, the set of input states is recreated one state at a time, and the operation \mathcal{S}_{op} of interest (in this paper the QFT) applied to each in turn. This gives a complete set of output states, $\{\rho_{\text{op}}\}$. Once again, readout of each ρ_{op} requires that the experiment be repeated followed by different readout operations $\{\mathcal{U}_{\text{ro}}\}$. The mean values of the complete set of observables $\{m_{\text{op}}\}$ that is measured allows reconstruction of the set of output states actually created. Finally, these estimates of $\{\rho_{\text{op}}\}$, together with the earlier estimates of $\{\rho_{\text{in}}\}$, are used to reconstruct an estimate of the operation \mathcal{S}_{op} via Eqn. (3). This reconstructed operation is not expected to be unitary due to decoherence during the application of \mathcal{S}_{op} as well as errors in the state tomography procedure. Also, due to incoherent errors across the ensemble involved in NMR experiments, the supermatrix \mathcal{M}_{obs} estimated via this QPT procedure may not correspond to a completely positive, trace preserving superoperator.

FIG. 3: Eigenvalues of simulated supermatrices in the complex plane. The main figure shows the location of the eigenvalues with respect to the unit circle, while the subplot shows the eigenvalue locations in greater detail. This simulation was done for alanine (see text),

and includes both coherent errors due to imperfect pulses and incoherent errors due to the inhomogeneous RF power across the sample. The eigenvalues indicated by circles (\circ) are of the product $\mathcal{S}_{180x}^{1,2} \mathcal{S}_{90y}^1$ of the supermatrix describing an evolution \mathcal{S}_{90y}^1 of a 90° pulse on spin 1 about the negative y-axis times a second supermatrix $\mathcal{S}_{180x}^{1,2}$ for a 180° rotation of spins 1 and 2 about the x-axis. The eigenvalues indicated by crosses (\times) are for the supermatrix $\mathcal{S}_{\text{both}}$ describing the net evolution after concatenating these pulses together in the simulator. Due to the presence of incoherence the eigenvalues are not the same. In particular, the presence of incoherence leads to an apparent decoherence, as evidenced by a reduction in the eigenvalue magnitudes. The average eigenvalue reduction is 1.2% for $\mathcal{S}_{\text{both}}$ and 0.9% for $\mathcal{S}_{180x}^{1,2} \mathcal{S}_{90y}^1$.

FIG. 4: The 33 point RF profile shows how much of the sample sees what fraction of the desired power (so 1.0 on the horizontal axis is the desired power). This profile was measured experimentally and used for the simulations.

FIG. 5: Measured Hadamard relaxation operator versus the product operator basis for the three carbons of alanine in the absence of RF fields, with rates color-coded as indicated by the legend. The labels on the axes are a short-hand for the product operators associated with with x and y directions on the three carbons, with e.g. $X1X \leftrightarrow \sigma_x^1 \sigma_x^3$. The labels for each entry of the matrix are obtained by analogy with the product rules for the Pauli operators; for example, the matrix entry in the row labeled $1XX$ and column labeled $Y1Y$ is $YZZ \leftrightarrow \sigma_y^1 \sigma_x^2 \sigma_z^3$ [23]. See Table I for the numerical values of the various entries.

FIG. 6: The various correlations (see Section II) for the 64 states of the product operator basis before and after applying the QFT, where those obtained from the uncompensated strongly modulating control sequences have been plotted against those obtained with the sequences designed to compensate for RF inhomogeneity [10]. To spread the points out, the (co)ordinates plotted are $\log_{10}(1+(1-x))$, although the axes have been labeled by the actual correlations $0 \leq x \leq 1$. Circles (\circ) are used for the initial state correlations, while triangles (\triangle) denote the final state correlations and stars (\star) indicate the final state attenuated correlations. For the uncompensated sequences the average initial state correlation is 0.93, the average final state correlation is 0.64, and the average attenuated correlation is 0.37. For the compensated sequences, the average initial state correlation is 0.96, the average final state correlation is 0.82, and the gate fidelity 0.64. Moreover, since a large majority of the points lie below the diagonal in the plot (dashed line), the correlations with the

compensated pulses were in fact better in almost every case.

FIG. 7: The bar graph on the left shows the amplitudes $a_k = \|A_k\|/\sqrt{8}$ of experimental QFT Kraus operators, where the light grey portions of the bars are the amplitudes obtained from QPT done with the uncompensated control sequences, and the dark grey bars those obtained from QPT done with the RF-compensated control sequences (see text). With the uncompensated control sequences the dominant Kraus operator had an amplitude $a_1^u = 0.72$, whereas the compensated had $a_1^c = 0.86$. The second largest Kraus operators had amplitudes of $a_2^u = 0.30$ and $a_2^c = 0.34$, respectively, after which the amplitudes decreased much more slowly. The plots on the right (which are shaded by column number to aid viewing) compare the real part of the desired unitary operator U_{QFT} (top center) to the real part of the largest Kraus operator A_1 obtained using the uncompensated and compensated control sequences (left and right-hand plots on the second row, respectively), and to the corresponding second largest Kraus operators A_2 (bottom row). The correlations between real parts of these operators were $C(\Re U_{\text{QFT}}, \Re A_1^u) = 0.78$, $C(\Re U_{\text{QFT}}, \Re A_1^c) = 0.95$, $C(\Re U_{\text{QFT}}, \Re A_2^u) = 0.06$ and $C(\Re U_{\text{QFT}}, \Re A_2^c) = 0.02$.

FIG. 8: The differences between the (attenuated) correlations of the output states and their mean values are displayed for each input state, which are indicated by the symbols on the left vertical axis with e.g. $1XY \leftrightarrow \sigma_x^2 \sigma_y^3$. The simulated-vs-theoretical state correlations are in blue, and the experimental-vs-theoretical state correlations are in yellow, while the corresponding attenuated correlations are in cyan and brown, respectively. The corresponding mean values of the (attenuated) correlations were 0.89, 0.82, 0.83 and 0.63, respectively. The pair of dashed vertical lines about the center mark one standard deviation for the input state correlations (not shown), which are expected to be determined primarily by measurement errors so that any values within these bounds are certainly almost entirely due to noise. The larger deviations in the correlations are due to the propagation of coherent error (see text), while the yet larger deviations in the attenuated correlations include the effects of decoherence (modeled as a uniform attenuation in the simulations).

FIG. 9: The left-hand plot shows the real amplitudes, of experimental QFT Kraus operators (dark grey) and those obtained from the QPT simulation based on the system-plus-apparatus model (light grey), where the negative values plotted are actually the negative square roots of one-eighth the absolute values of the corresponding Choi matrix eigenvalues. It may be seen that the experimental deviated significantly more from being completely

positive than the simulated, most likely to the absence of errors from fitting the spectra in the latter (see text). The dominant Kraus operator has an amplitude 0.86 for the experiment and 0.87 for the model. The right side of the figure compares the real part of the theoretical unitary QFT operator (top-middle) to the largest Kraus operator from the experiment (middle-left) and simulated (middle-right) supermatrices. Also shown are the real parts of the corresponding best unitary approximations to these largest Kraus operators (bottom line). The correlation between the two largest Kraus operators, and between the corresponding best unitary approximations, was 0.90 in both cases.

FIG. 10: The theoretical (left), simulated (middle) and experimental (right) supermatrices of the QFT in the phase space basis, wherein all their elements are necessarily real. Since the theoretical is simply a permutation matrix in this basis, the differences between it and the other two are easily seen, but the physical meanings of these differences are obscure. For example, the level of “background noise” is noticeably larger in the simulation than in the experiment, although both have the maximum entry of each row (column) in the same place as the theoretical.

FIG. 11: The real parts of the theoretical (left), simulated (middle) and experimental (right) supermatrices in the computational (Zeeman) basis, where the theoretical superoperator is given in terms of the unitary operator by $\overline{U}_{\text{th}}^{\text{QFT}} \otimes U_{\text{th}}^{\text{QFT}}$. The correlations and attenuated correlations among these matrices may be found in Table II. Although the pattern of the theoretical superoperator’s matrix elements is visible in both the simulated and the experimental supermatrix, it is still not at all obvious from this vantage point what errors have occurred during implementation or how they can be corrected.

FIG. 12: The theoretical (left), simulated (middle) and experimental supermatrices in the product operator basis, wherein all the elements are necessarily real (see text; the scale has been reduced by a factor of 2 to create more contrast). The correspondence between the rows / columns of this supermatrix and the individual product operators is the same as that given by the labels on the vertical axis of the bar graph in Fig. 8. Because all the entries of the corresponding “real” density matrix are the expectation values of observables which transform nicely under rotations [23], the physical interpretation is somewhat easier in this basis. This is manifest, for example, in the appearance of several fixed points with a 1 on the diagonal and zeros elsewhere in the same row (see text).

FIG. 13: Theoretical (left), simulated (middle) and experimental (right) supermatrices in

the phase space basis after correcting the latter two by a unitary supermatrix designed to bring them as close as possible to the theoretical (as described in the text). The levels of background noise are a great deal less than in the corresponding uncorrected supermatrices (Fig. 10).

FIG. 14: As may be seen from row 14 of the supermatrices shown in Fig. 12, the operator $\sigma_x^1 \sigma_z^3$ is a fixed point of the QFT. The upper bar graph displays the corresponding row of the theoretical (dark grey), simulated (medium grey) and simulated with coherent errors corrected (light grey) supermatrix elements versus the product operator basis, whereas the lower bar graph displays these same statistics for the experimental supermatrix. In contrast to the phase space and Zeeman basis (not shown), there is a significant correlation between the experimental and simulated values; specifically, the simulated-to-experimental correlation coefficients were 0.80 and 0.94 before and after correction, respectively. In the present case these correlations are due almost entirely to the single large diagonal value, but similar correlations were obtained for all other pairs of rows; the average correlations were 0.78 and 0.94 before and after correction, respectively.

FIG. 15: Plot of the eigenvalues of simulated QFT superoperators in the complex plane, specifically, the results of simulations with only coherent errors (blue “○”), the results including relaxation using the relaxation superoperator shown in Fig. 5 and Table I (red “*”), the results including incoherent errors but no relaxation (cyan “●”), and the same following simulation of the full QPT procedure (green “×”), wherein decoherence was mimicked simply by scaling down the simulated QFT superoperators following the state readout pulses by a factor of 0.82 (save for the component with eigenvalue 1, which is needed for trace-preservation). To aid the comparison, the eigenvalues of the QFT superoperator including only the coherent errors (blue “○”) were scaled to have the same RMS value as those obtained with the simulated relaxation, thereby showing that the net effect of relaxation on the results of the QFT is simply to lower the amplitude of the eigenvalues without otherwise dispersing them in the complex plane. It may also be seen that the effect of incoherent errors on the eigenvalues is both to increase their angular spread and scale them down proportionately, so that they tend to move along arcs inside of and tangent to the unit circle, and that the additional errors introduced by the tomography procedure do not alter them greatly.

FIG. 16: The blue squares (□) are the eigenvalues of the simulated supermatrix \mathcal{M}_{sim} ,

including coherent, incoherent and readout errors, while the magenta triangles (\triangle) are those after correcting \mathcal{M}_{obs} by post-multiplication with the product of single-spin rotations $U_{\Delta}^1 \otimes U_{\Delta}^2 \otimes U_{\Delta}^3$ and the orange diamonds after pre-multiplication with a product of different single-spin rotations (see Table III). Although we cannot quite unambiguously match up pairs of eigenvalues, it is clear that they have been made very similar by these corrections.

FIG. 17: The blue plus-signs (\oplus) are the eigenvalues of the experimental supermatrix \mathcal{M}_{obs} , while the red five-pointed stars (\star) are those of its best completely positive and trace-preserving approximation $\mathcal{M}_{\text{CPTP}}$, and the green six-pointed stars (\blacklozenge) are those of the superoperator corresponding to the best unitary approximation to its largest Kraus operator $\bar{U}_{1,\text{CPTP}} \otimes U_{1,\text{CPTP}}$ (see text), scaled down to have the same trace as $\mathcal{M}_{\text{CPTP}}$.

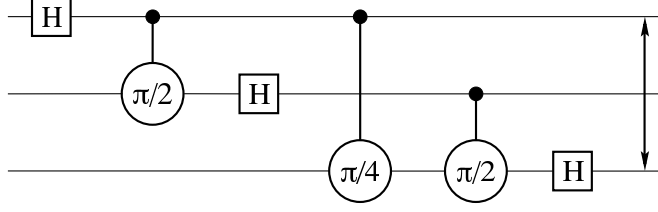
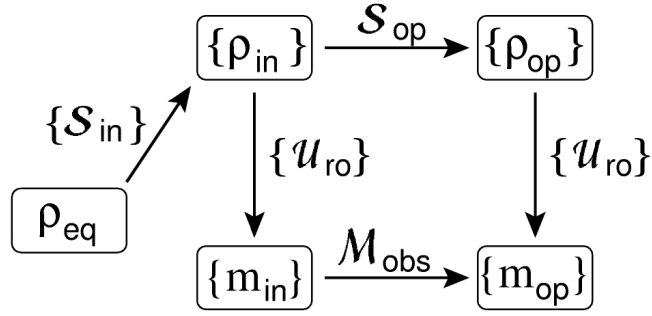


FIG. 1



$$\mathbf{u}_{\text{ro}}(\rho) \equiv \int dq U_{\text{ro}}^{(q)} \rho U_{\text{ro}}^{(q)\dagger}$$

$$m_{\text{xx}} \equiv \text{tr}(\mathbf{u}_{\text{ro}}(\rho_{\text{xx}}) \sigma_-)$$

FIG. 2

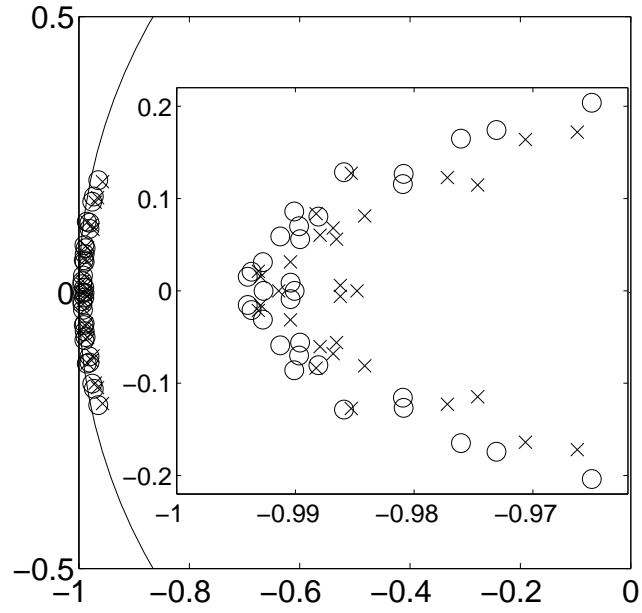


FIG. 3

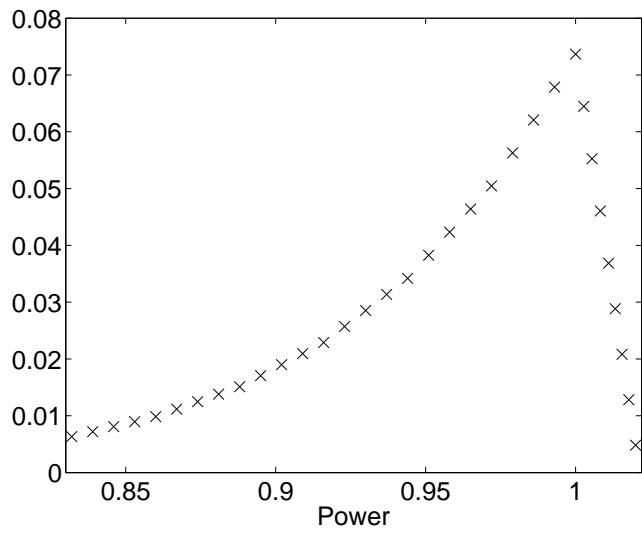


FIG. 4

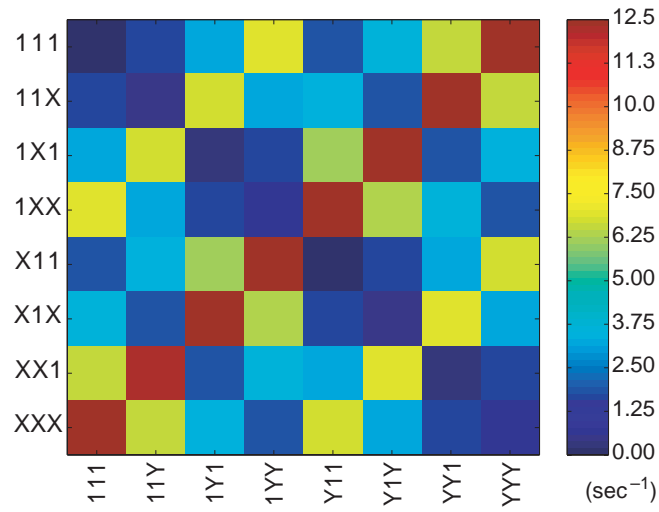


FIG. 5

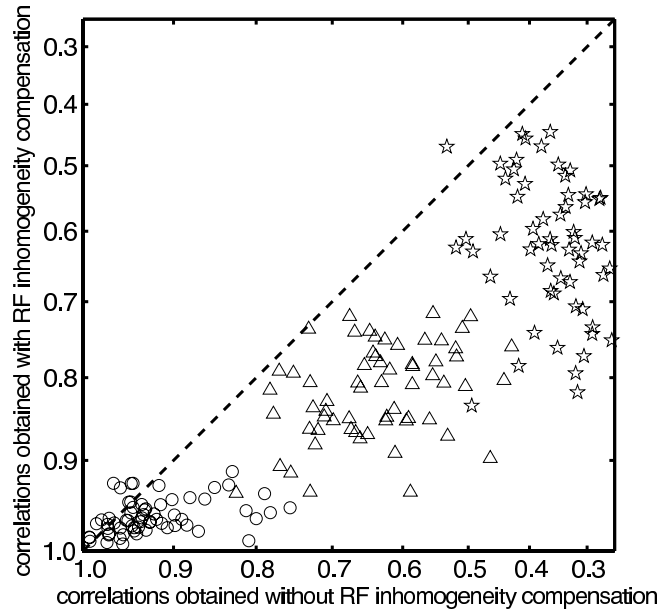


FIG. 6

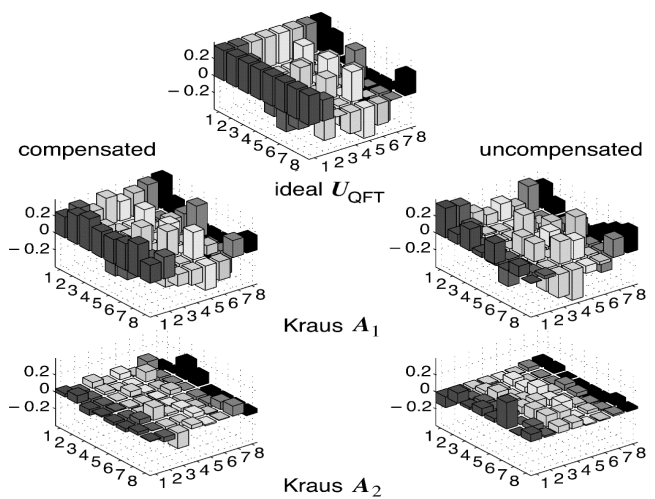
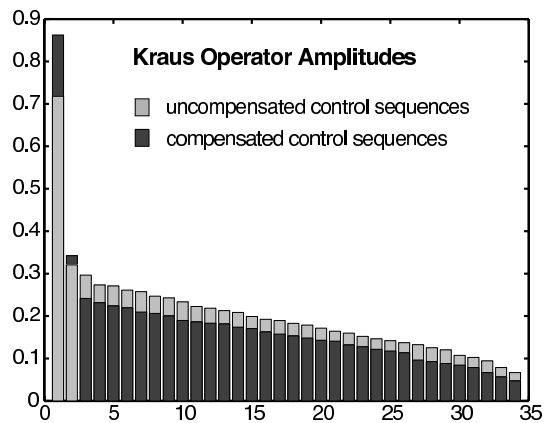


FIG. 7

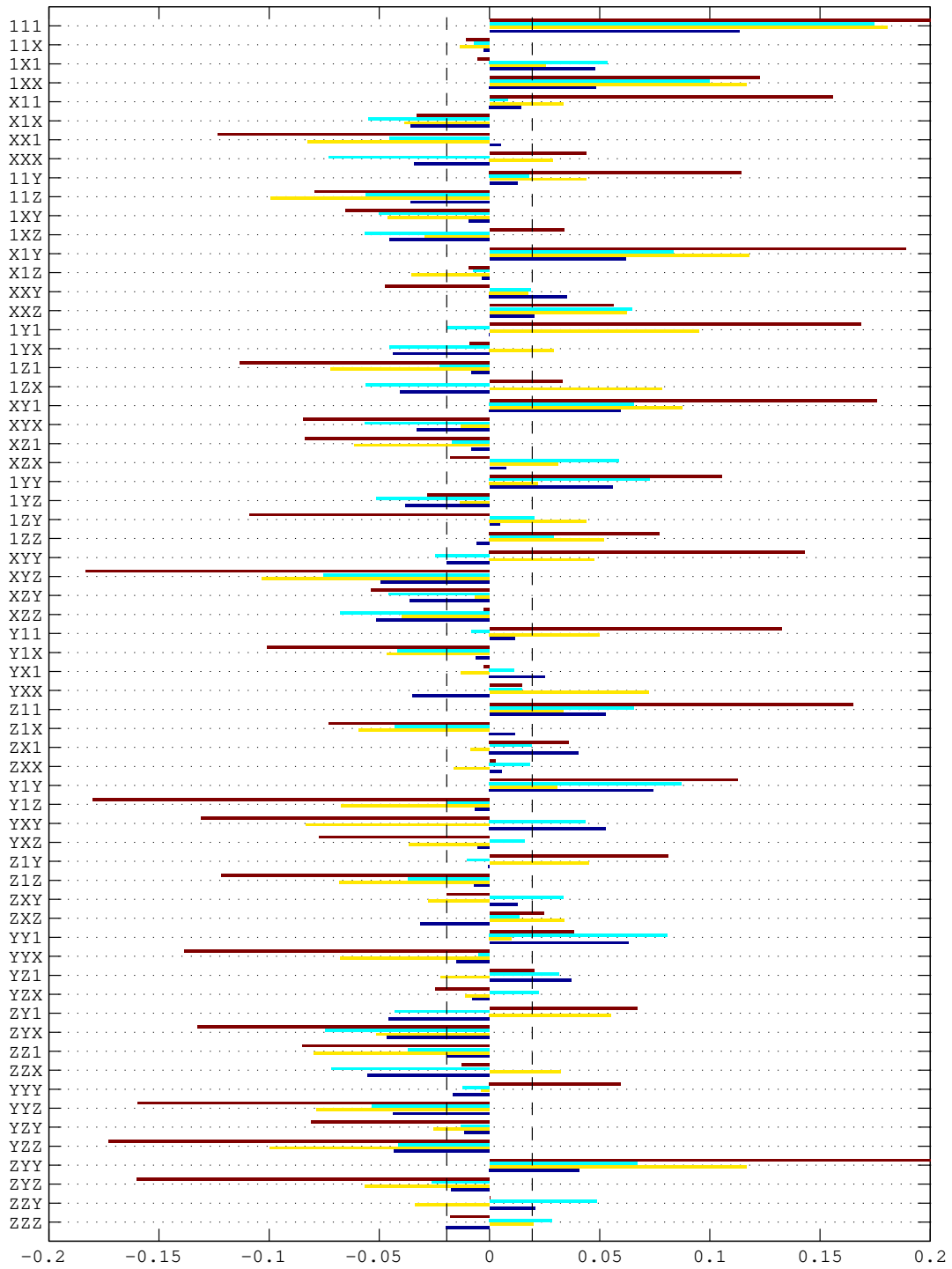


FIG. 8

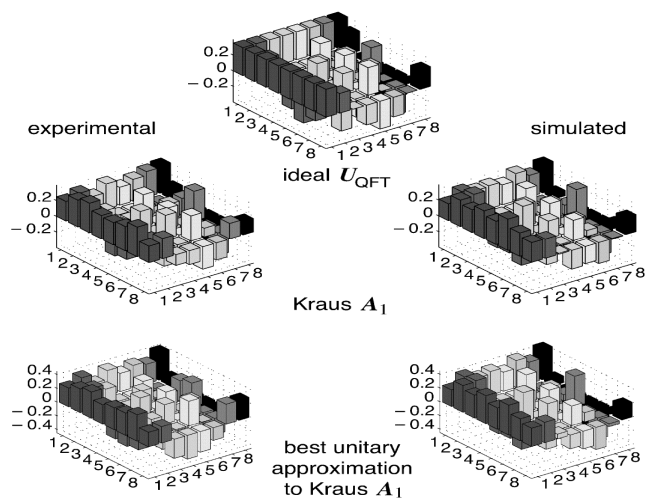
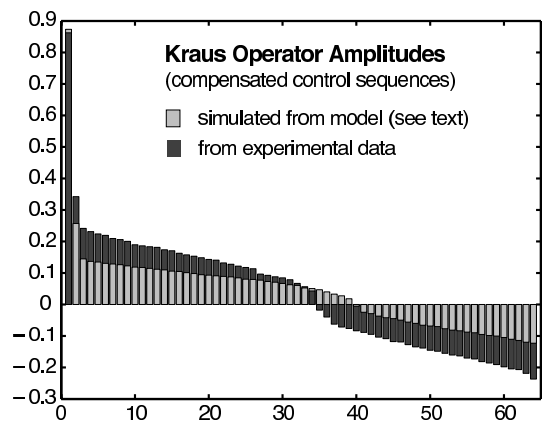


FIG. 9

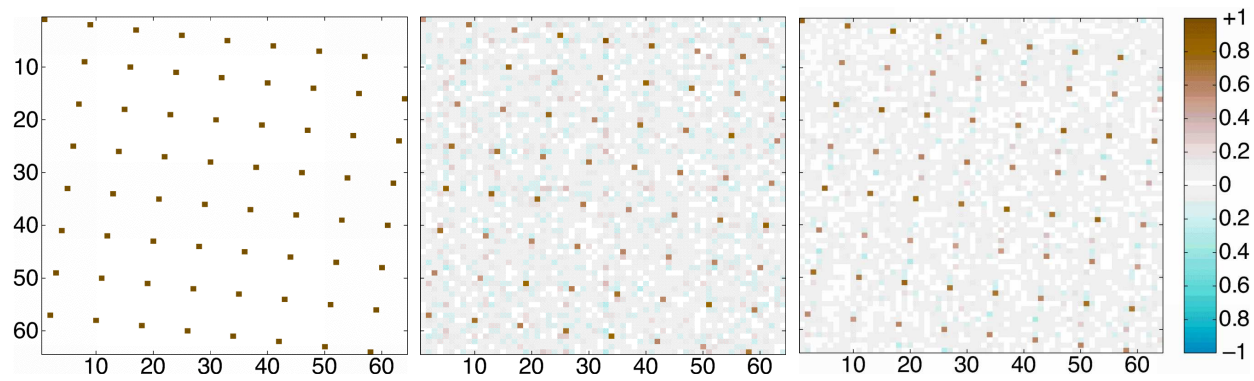


FIG. 10

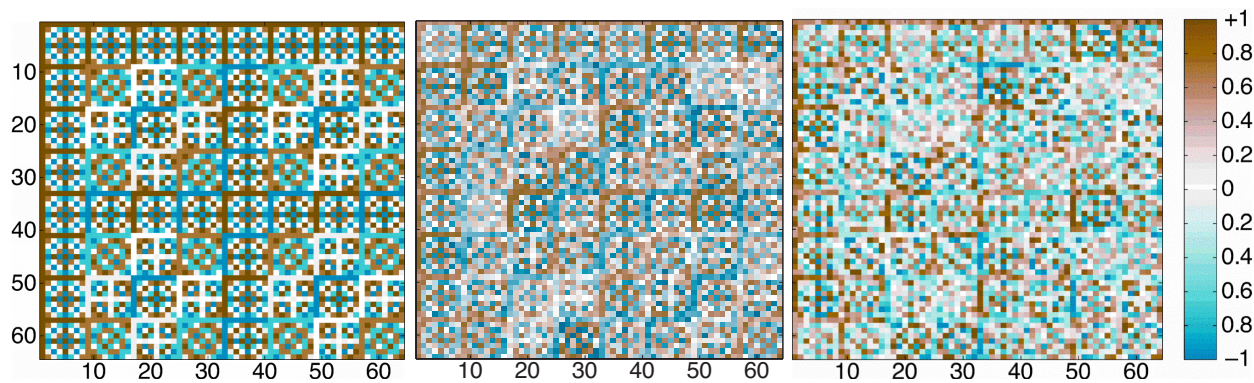


FIG. 11

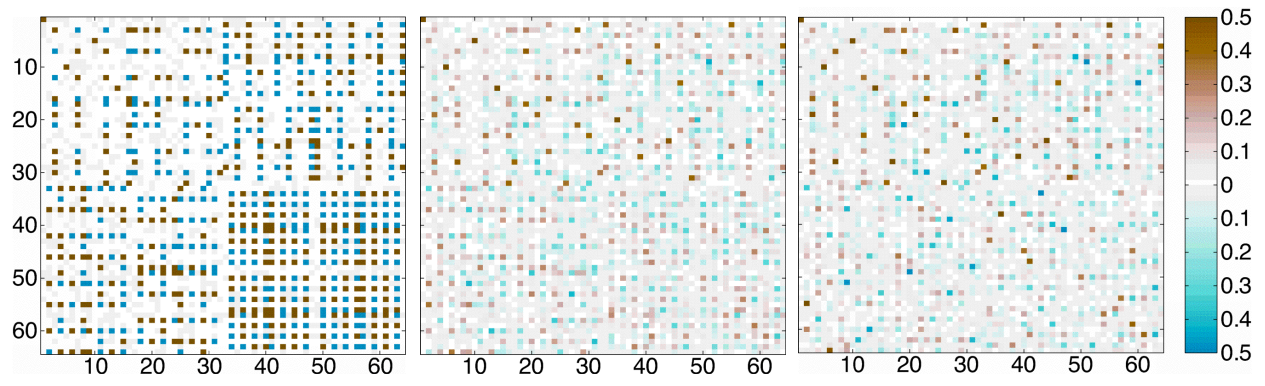


FIG. 12

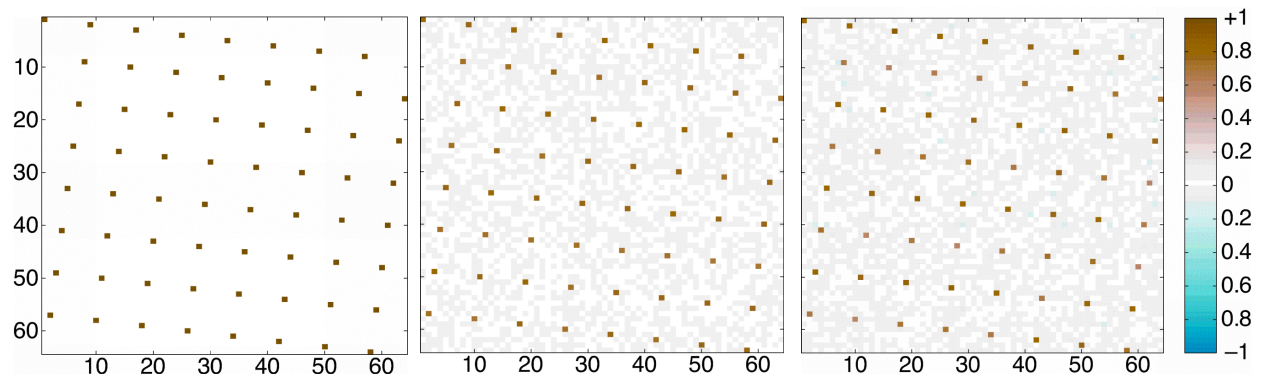


FIG. 13

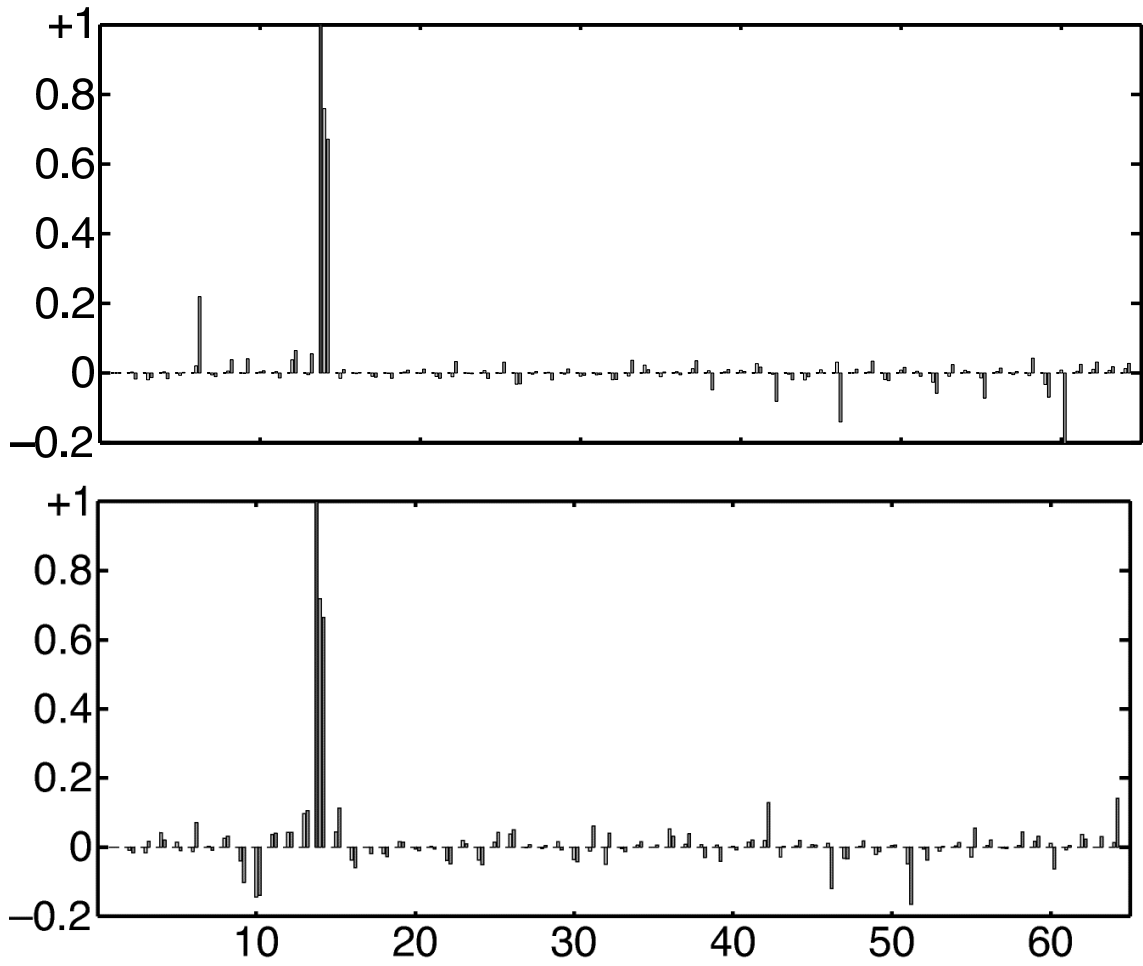


FIG. 14

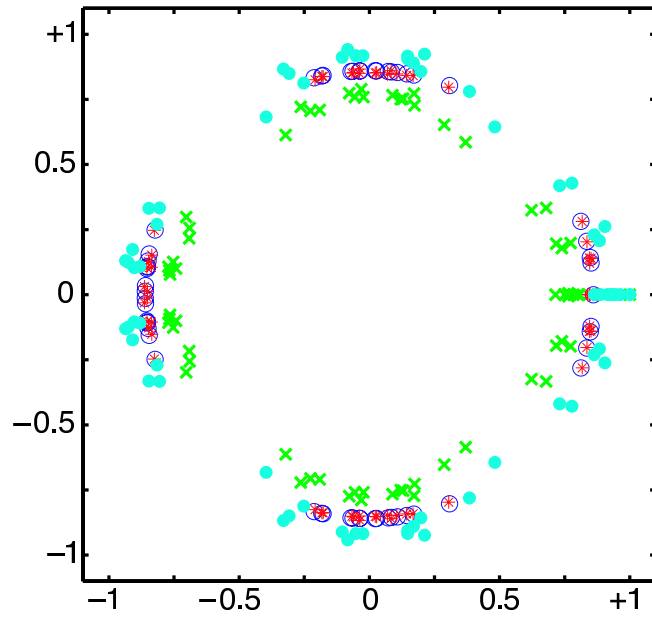


FIG. 15

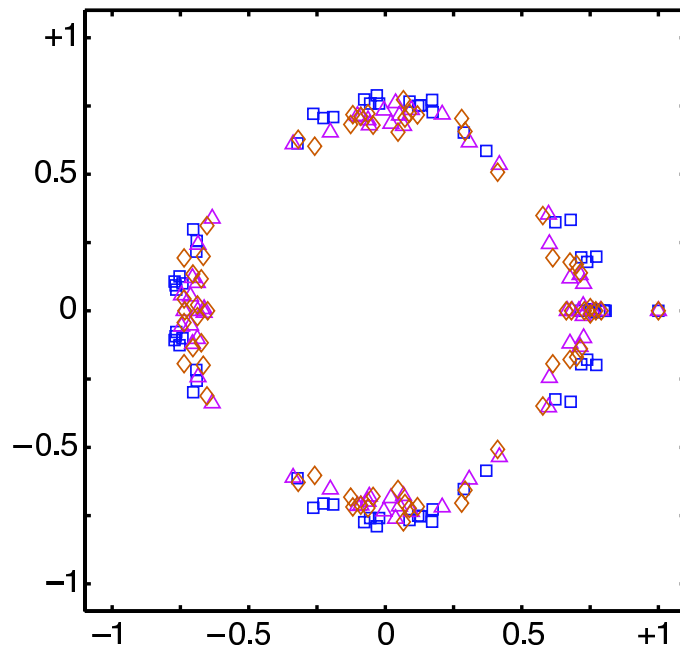


FIG. 16

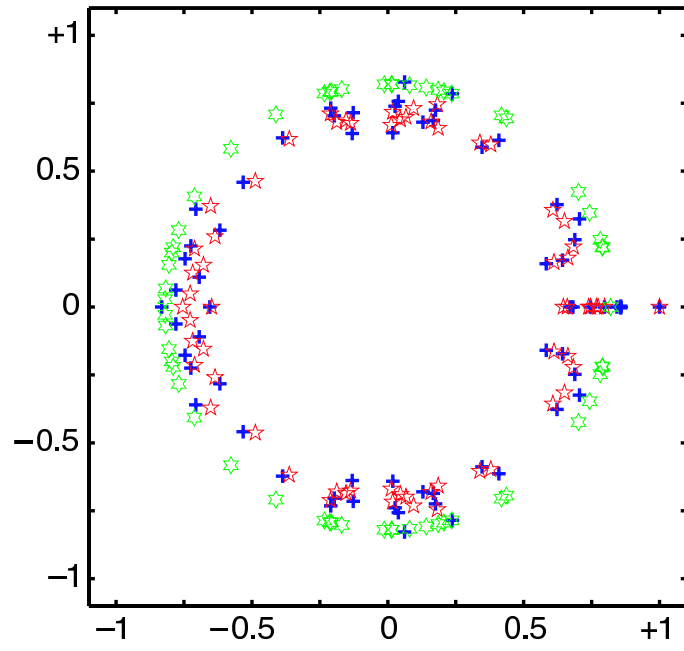


FIG. 17